



## Femtochemistry of bimolecular reactions from weakly bound complexes

Computational study of the  $\text{H} + \text{H}'\text{OD} \rightarrow \text{H}'\text{OH} + \text{D}$  or  $\text{HOD} + \text{H}'$  exchange reactions

Voute, Alexandre; Gatti, Fabien; Møller, Klaus B.; Henriksen, Niels E.

*Published in:*  
Physical Chemistry Chemical Physics

*Link to article, DOI:*  
[10.1039/d1cp04391a](https://doi.org/10.1039/d1cp04391a)

*Publication date:*  
2021

*Document Version*  
Peer reviewed version

[Link back to DTU Orbit](#)

*Citation (APA):*  
Voute, A., Gatti, F., Møller, K. B., & Henriksen, N. E. (2021). Femtochemistry of bimolecular reactions from weakly bound complexes: Computational study of the  $\text{H} + \text{H}'\text{OD} \rightarrow \text{H}'\text{OH} + \text{D}$  or  $\text{HOD} + \text{H}'$  exchange reactions. *Physical Chemistry Chemical Physics*, 23(48), 27207-27226. <https://doi.org/10.1039/d1cp04391a>

---

### General rights

Copyright and moral rights for the publications made accessible in the public portal are retained by the authors and/or other copyright owners and it is a condition of accessing publications that users recognise and abide by the legal requirements associated with these rights.

- Users may download and print one copy of any publication from the public portal for the purpose of private study or research.
- You may not further distribute the material or use it for any profit-making activity or commercial gain
- You may freely distribute the URL identifying the publication in the public portal

If you believe that this document breaches copyright please contact us providing details, and we will remove access to the work immediately and investigate your claim.

Cite this: DOI: 00.0000/xxxxxxxxxx

# Femtochemistry of bimolecular reactions from weakly bound complexes: computational study of the $\text{H} + \text{H}'\text{OD} \longrightarrow \text{H}'\text{OH} + \text{D}/\text{HOD} + \text{H}'$ exchange reactions

Alexandre Voute,<sup>a</sup> Fabien Gatti,<sup>b</sup> Klaus B. Møller<sup>a</sup> and Niels E. Henriksen<sup>\*a</sup>

Received Date

Accepted Date

DOI: 00.0000/xxxxxxxxxx

A full-dimensional wavepacket propagation describing the bimolecular exchange reactions  $\text{H} + \text{H}'\text{OD} \longrightarrow \text{H}'\text{OH} + \text{D}/\text{HOD} + \text{H}'$  initiated by photolysis of HCl in the hydrogen-bound complex  $(\text{HCl}) \cdots (\text{HOD})$  is reported. The dynamics of this reaction is carried out with the MCTDH method on an *ab initio* potential energy surface (PES) of  $\text{H}_3\text{O}$  and the initial state is derived from the ground state wavefunction of the complex obtained by relaxation on its own electronic ground state *ab initio* PES. The description of the system makes use of polyspherical coordinates parametrizing a set of Radau and Jacobi vectors. The calculated energy- and time-resolved reaction probabilities show, owing to the large collision energies at play stemming from the (almost full) photolysis of HCl, that the repulsion between oxygen in the  $\text{H}'\text{OD}$  molecule and the incoming hydrogen atom is the main feature of the collision and leads to non-reactive scattering. No abstraction reaction products are observed. However, both exchange processes are still observable, with a preference in O–H' bond dissociation over that of O–D. The selectivity is reversed upon vibrational pre-excitation of the O–D stretching mode in the  $\text{H}'\text{OD}$  molecule. It is shown that, after the collision, the hydrogen atom of HCl does most likely not encounter the almost stationary chlorine atom again but we also consider the limit case where the H atom is forced to collide multiple times against  $\text{H}'\text{OD}$  as a result of being pushed back by the Cl atom.

## 1 Introduction

The vast majority of chemical reactions rely on the encounter between molecules. At the elementary molecular level, the collision between two molecules, possibly giving rise to new compounds, is the basic phenomenon where molecules exchange atoms and energy.<sup>1</sup> As is known, the outcome of a single bimolecular collision depends on the initial quantum state of the reactants and the shape of the potential energy surface (PES) in which they lie. Other conditions are also crucial, such as their relative orientations, the collision impact parameter and the relative translational kinetic energy.

Molecular crossed-beam scattering experiments,<sup>2–5</sup> where a molecule conveyed in one beam with a selected translational kinetic energy scatters due to the sole interaction with a single molecule from the other beam, provide a deep understanding of bimolecular reactions. In these specific conditions, one can quantify the energy required for a given reaction to succeed, characterize whether a collision is elastic or inelastic and, in the latter

case, determine how energy is redistributed within the molecules. Yet, the influence of the relative orientations and the impact parameter on the outcome of these collisions can not be readily discerned, as the molecules in the beam are randomly distributed. With the emergence of 'transition state spectroscopy',<sup>6,7</sup> the nature of the reaction in the vicinity of the barrier could be elucidated for some cases by fixing these geometrical aspects. One of the methods used to achieve this geometrical restriction is to form weakly-bound complexes of the reactants.

The use of weakly bound atom-molecule aggregates in chemical reactions can be traced back to the work of Jouvot and Soep<sup>8</sup> who studied the photochemistry of the  $\text{Hg} \cdots \text{Cl}_2$  atom-molecule van der Waals complex. Later, complexes of two molecules were used by Wittig et al. such as  $(\text{HBr}) \cdots (\text{CO}_2)$ <sup>9,10</sup>,  $(\text{H}_2\text{S}) \cdots (\text{CO}_2)$ <sup>11</sup>,  $(\text{HI}) \cdots (\text{CO}_2)$ <sup>12</sup>,  $(\text{N}_2\text{O}) \cdots (\text{HI})$ <sup>13</sup>,  $(\text{OCS}) \cdots (\text{DI})$ <sup>14</sup>. These groups took the advantage of bringing different molecules close to each other thanks to their weak mutual interaction, ranging from van der Waals interactions to the stronger hydrogen-bonds. It is then by irradiating the formed complex with light that they would trigger a reaction involving the two moieties. In the case of two molecules A–B and C, one forms the weakly bound complex  $\text{A}–\text{B} \cdots \text{C}$ , then irradiates the system with light so as to photodissociate A–B. As

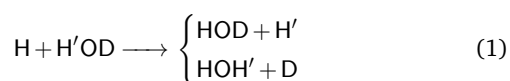
<sup>a</sup> Department of Chemistry, Technical University of Denmark, Kemitorvet 206, 2800 Kongens Lyngby, Denmark. E-mail: neh@kemi.dtu.dk

<sup>b</sup> ISMO, Institut des Sciences Moléculaires d'Orsay - UMR 8214 CNRS/Université Paris-Saclay, F-91405 Orsay, France

a result, the fragment A is ejected away from the whole system and B is thrown against C. The collision of B with C is then the bimolecular elementary process of interest. What is special here is that the initial positions of the colliding molecules are given by the geometry of the starting complex and that the collisional process takes place in the electronic ground state of the latter, provided that the fragment A is far enough from the two others, B + C, and that B is formed in its electronic ground state.

In these works, the measured physical quantities were given as functions of the photodissociating continuous wave laser frequency, preventing the observation of time-dependent quantities. Eventually, sub-picosecond time-resolved analysis of bimolecular reactions from predefined initial conditions were accomplished by Zewail and collaborators who exploited the idea of using weakly bound complexes in pump-probe laser femtochemistry experiments. Here, a first short laser pulse ('pump') initiates the process by photodissociating one of the molecules of the complex (in the example above, A – B), thus setting a 'zero of time' of the reaction to be observed. A second, delayed, laser pulse ('probe') is beamed on the system. The response of the latter by interaction with the probe pulse gives then an indication of the status of the system at a given time after the pump pulse. This procedure is ubiquitous in Zewail's pioneering work and has been applied to a large number of studies of more common unimolecular dynamics. The situation described here is conceptually the same if one considers the complex as a single 'supermolecule' where the collisional process unfolds internally. The first experiments of this kind carried out by Zewail's group involved the complexes (HI)⋯(CO<sub>2</sub>)<sup>15,16</sup> and (HBr)⋯(I<sub>2</sub>)<sup>17,18</sup>. Since then, this and other groups explored or revisited this class of reactions<sup>19–24</sup> and similar ones relying on charge transfer between the moieties of the complex upon photoexcitation by the pump pulse.<sup>25–30</sup>

One of the prototypical examples of bimolecular reactions is the pair of exchange reactions:



These exchange reactions have been studied only from a theoretical standpoint,<sup>31–36</sup> whereas the competing 'abstraction' reactions  $\text{H} + \text{H}'\text{OD} \longrightarrow \text{HH}' + \text{DO}$  or  $\text{HD} + \text{H}'\text{O}$  have received a lot of attention in both theory<sup>4,31–36</sup> and experiments.<sup>4,37–42</sup> In the context of the ideas explained above, we explore, in this paper, the possibility of initiating the exchange reactions (1) starting from the hydrogen-bound complex (HCl)⋯(HOD) by breaking the HCl moiety with an appropriate short laser pulse. The approach we adopt is based on quantum mechanics where we solve numerically the time-dependent Schrödinger equation (TDSE) for the nuclear wavefunction, aiming at predicting how the nuclei involved in the reaction will move. In particular, one of our main goals here is to calculate time-dependent reaction probabilities along the exchange and recoil channels of the above-mentioned reaction. To the best of our knowledge, no time-resolved experiments on that exchange reactions and no study of such reactions occurring from the use of the (HCl)⋯(HOD) complex seem to have ever been conducted. With this paper, our hope is to revive

the interest in the femtochemistry of these 'precursor-initiated' bimolecular reactions, which have received attention from experimentalists until twenty years ago but have lacked theoretical studies.<sup>43</sup> As will be shown, the development of new accurate *ab initio* PESs and efficient algorithms for solving the TDSE in recent years have made it possible to come back to these.

We structure this work as follows. First, we will briefly review the existing work regarding the (HCl)⋯(HOD) complex and the photodissociation of HCl. Next, we explain how the nuclear coordinates of the reacting system  $\text{H} + \text{H}'\text{OD}$  are described in terms of polyspherical coordinates whose choice determines the form of the kinetic energy operator to be used. Subsequently, we will be in the position of specifying the initial state used for the time propagation given the assumptions invoked in this study. Details on the computational aspects of the simulations are then provided. Finally, we present and discuss the results we have obtained.

## 2 The starting complex (HCl)⋯(HOD) and the photodissociation of HCl

The complex (HCl)⋯(H<sub>2</sub>O) and its various isotopologues are known in the literature. Experimentalists could observe it in a variety of conditions by many methods, including Fourier transform microwave (FTMW) spectroscopy in supersonic jets,<sup>44–46</sup> Fourier transform infrared (FTIR) spectroscopy in supersonic jets,<sup>47,48</sup> inert matrices<sup>49–54</sup> and Helium nanodroplets,<sup>55–57</sup> time-of-flight mass spectrometry and velocity-map imaging used to observe vibrational predissociation of the complex<sup>58,59</sup> and infrared cavity ringdown spectroscopy.<sup>60,61</sup> Many theoretical analyses using *ab initio* electronic structure methods<sup>62–76</sup> were published as well.

It is established that HCl is the hydrogen-bond donor in the binary complex while remaining non-ionized. *Ab initio* methods indicate the existence of three noteworthy stationary points on the potential energy surface. Two of them are identical global minima with *C<sub>s</sub>* geometries (as in fig. 1), one being the image of the other by reflection through the plane of the water molecule. The other one is a saddle point with planar *C<sub>2v</sub>* geometry (where HCl and H<sub>2</sub>O are now coplanar) connecting the two minima and whose imaginary frequency normal mode is the oscillation between one such geometry to the other. The minimum energy path on the PES going through these three points describes a double-well potential curve. However, the barrier between the two *C<sub>s</sub>* geometries turns out to be smaller than the vibrational zero-point energy. As a consequence, the vibrational ground state wavefunction is delocalized over that double-well and the planar *C<sub>2v</sub>* geometry is the most likely to be observed. With the calculation of the potential energy surface for this system at the CCSD(T)/aug-cc-pvtz level of theory, Mancini and Bowman could accurately calculate the barrier height and obtain the vibrational ground state wavefunction and zero-point energy by the diffusion Monte Carlo method.<sup>73</sup>

Excited states potential energy surfaces of the complex, in particular of (HCl\*)⋯(H<sub>2</sub>O) where HCl dissociates, are instead not available. However, the photodissociation of HCl alone is known and is not expected to differ much when occurring within the complex because of the relatively weak bond between the water molecule and the hydrogen halide. This aspect will be further dis-

cussed when defining the initial state. According to the work of Schmidt *et al.*,<sup>77</sup> the first allowed electronic transition originating from the electronic ground state  $X^1\Sigma$  is the  $A^1\Pi \leftarrow X^1\Sigma$ , with vertical energy 7.9274 eV corresponding to 156.40 nm. When corrected with the vibrational zero-point energy of HCl,<sup>78</sup> the effective vertical transition energy becomes 7.7434 eV, corresponding to 160.12 nm. The potential curve of the  $A^1\Pi$  state is characteristic of an exponential-decay-like unbound state correlating to ground state  $\text{Cl}(^2P)$  and  $\text{H}(^2S)$ . The difference  $\Delta V_{\text{exc}}$  in energy between the Franck-Condon geometry and the infinitely separated Cl and H is  $\Delta V_{\text{exc}} = 3.2825$  eV. Were these two atoms considered as classical particles, by conservation of momentum they would then gain opposite partial momenta of magnitude  $p_{\text{exc}} = \sqrt{2\mu\Delta V_{\text{exc}}}$ , as shown in appendix A. It is important to note that these quantities are given in the space-fixed frame of reference of HCl.

These considerations, will be important for the definition of the initial state of  $\text{H} + \text{HOD}$ , as will be done in section 4. In order to be specific, we first discuss in the following section how nuclear configurations are defined in this study.

### 3 Choice of coordinates and Hamiltonian

As in any many-body dynamical problem, the choice of the coordinates describing the system is crucial. A balance has to be found between convenience (for analysis and interpretation of the results) and tractability of the equations of motion. In molecules, the nuclei move with respect to one another, so that distances between pairs of them and various angles are, at first sight, the most natural coordinates to choose. It turns out that this very choice is not optimal in general, in particular when molecules contain more than three atoms. Indeed, distance vectors do not yield a convenient kinetic energy operator to work with, as the number of terms coupling the conjugated momenta associated to each vector scales with the square of the number of atoms. However, one can judiciously work with another set of vectors which, by design, make these crossed terms disappear. Such vectors, in the context of molecular many-body dynamics, are called ‘orthogonal vectors’ (this does *not* mean they are perpendicular) since they ‘diagonalize’ the kinetic energy operator. By this we mean that the kinetic energy is expressed simply as the sum of momenta squared (weighted by their associated masses) without mixed terms. For this reason, as detailed in the following, we choose a non-trivial set of orthogonal vectors to describe the molecular system. These are parametrized in spherical coordinates and, by the polyspherical approach,<sup>79</sup> we find the expression of the kinetic energy operator used in this study.

From now on, we call  $\text{H}_a$  the hydrogen atom belonging to HCl and  $\text{H}_b$  the one belonging to HOD (see fig. 1).  $G$  is the center of mass of  $\text{H}_a\text{H}_b\text{OD}$ ,  $G_s$  is the center of mass of the *subsystem*  $\text{H}_b\text{OD}$  and  $K$  is its so-called ‘canonical point’ with O being the heliocenter, as defined by Radau.<sup>80,81</sup> These points are defined

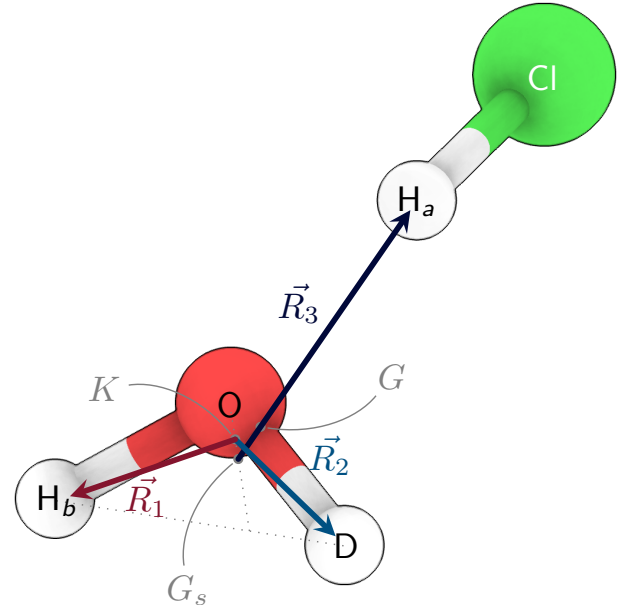


Fig. 1 Minimum potential energy geometry of the  $(\text{HCl})\cdots(\text{HOD})$  complex and the vectors describing the relative positions of the atoms  $\text{H}_a$ ,  $\text{H}_b$ , D and O. The shown points are:  $G$ , the center of mass of  $\{\text{H}_a, \text{H}_b, \text{D}, \text{O}\}$ ;  $G_s$ , the center of mass of the *subsystem*  $\{\text{H}_b, \text{D}, \text{O}\}$ ;  $K$ , the Radau canonical point of  $\{\text{H}_b, \text{D}, \text{O}\}$  with heliocenter  $O$ . Some lengths are exaggerated for visualization purposes (to make  $G$ ,  $G_s$  and  $K$  distinguishable).

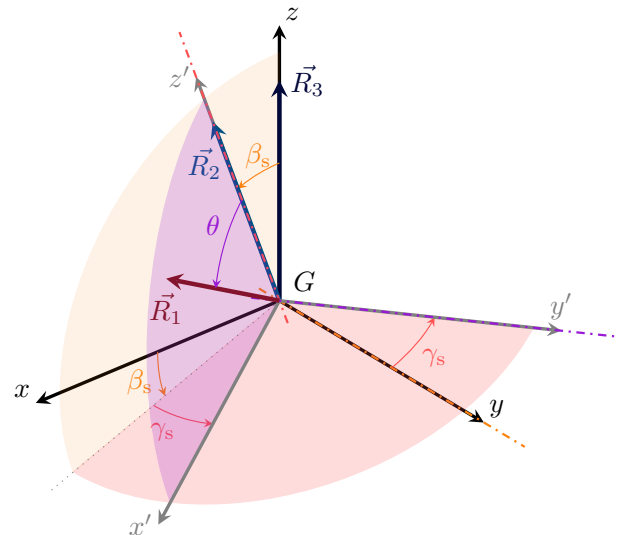


Fig. 2 The three vectors  $\vec{R}_1$ ,  $\vec{R}_2$  and  $\vec{R}_3$  of fig. 1 and definition of the angles  $\beta_s$ ,  $\gamma_s$  and  $\theta$  between them in the BF and BF's frames of reference. The coordinate system  $(Gxyz)$  is attached to the body-fixed frame BF, whereas  $(Gx'y'z')$  is attached to the ‘subsystem’-body-fixed frame BF's. In the text,  $u = \cos \theta$

such that:

$$\vec{x}_G = \frac{m_H \vec{x}_{H_a} + m_H \vec{x}_{H_b} + m_O \vec{x}_O + m_D \vec{x}_D}{2m_H + m_O + m_D} \quad (2)$$

$$\vec{x}_{G_s} = \frac{m_H \vec{x}_{H_b} + m_O \vec{x}_O + m_D \vec{x}_D}{m_H + m_O + m_D} \quad (3)$$

$$\vec{x}_K - \vec{x}_O = (1 + \alpha_O)^{-1} (\vec{x}_{G_s} - \vec{x}_O) \quad (4)$$

$$\alpha_O = \sqrt{\frac{m_O}{m_H + m_O + m_D}} \quad (5)$$

Since we are not interested in the fate of the chlorine atom after HCl has dissociated, the wavefunction for which we will solve the time-dependent Schrödinger equation will not depend on its coordinates. As will be shown later, these will play a role only in obtaining the initial state in the computations. We focus here on the other atoms of the molecular system  $H_a + H_bOD$ , shown in fig. 1 with the points we have just defined. The relative positions of these four atoms are given by three vectors  $\vec{R}_1$ ,  $\vec{R}_2$  and  $\vec{R}_3$ , also shown in the figure and defined as follows:

$$\vec{R}_1 = \vec{x}_{H_b} - \vec{x}_K \quad (6)$$

$$\vec{R}_2 = \vec{x}_D - \vec{x}_K \quad (7)$$

$$\vec{R}_3 = \vec{x}_{H_a} - \vec{x}_{G_s} \quad (8)$$

We call  $\alpha$ ,  $\beta$  and  $\gamma$  the three Euler angles of the overall rotation of the system. The rotating body-fixed (BF) frame of reference is chosen such that its  $z$ -axis is aligned along the  $\vec{R}_3$  vector and the  $x$ -axis is in the plane defined by  $\vec{R}_2$  and  $\vec{R}_3$  (with  $\vec{R}_2$  being oriented towards positive  $x$ ). By this choice,  $\alpha$  and  $\beta$  are given by the spherical angles of  $\vec{R}_3$  with respect to a given lab frame of reference and  $\gamma$  is defined in such a way that (for small values  $\gamma$ )  $\vec{R}_2$  lies in the  $(xz, x > 0)$  semi-plane. As will be clearer later, we write  $\gamma = \alpha_s$  for convenience. Finally, as shown in fig. 2, we call  $\beta_s$ ,  $\gamma_s$  and  $\theta$  the angle from  $\vec{R}_3$  to  $\vec{R}_2$ , the rotation angle of  $\vec{R}_1$  around  $\vec{R}_2$  and the angle from  $\vec{R}_2$  to  $\vec{R}_1$ , respectively. We define for convenience a ‘subsystem’-body-fixed (BFs) frame of reference attached to  $H_bOD$ , whose  $z'$ -axis is aligned along  $\vec{R}_2$  and the  $x'$ -axis is such that (for small values of  $\theta$ )  $\vec{R}_1$  is in the  $(x'z', x' > 0)$  semi-plane. As the Euler angles  $\alpha$ ,  $\beta$  and  $\gamma = \alpha_s$  define the overall orientation of the system, they will be called ‘external’ coordinates, as opposed to  $R_1$ ,  $R_2$ ,  $R_3$ ,  $\beta_s$ ,  $\gamma_s$  and  $\theta$  which will be called ‘internal’ coordinates ( $R_k = \|\vec{R}_k\|, k \in \{1, 2, 3\}$ ).

$\vec{R}_1$ ,  $\vec{R}_2$  (which are Radau vectors within  $H_bOD$ ) and  $\vec{R}_3$  (Jacobi vector) are said to be ‘orthogonal’ in the sense that the classical expression of the kinetic energy in the space-fixed frame of reference of  $H_aH_bOD$  (i.e. whose origin is the center of mass  $G$  and the axes do not rotate with respect to any given lab-fixed frame of reference) is a linear combination of the squares of their conjugate momenta  $\vec{P}_1$ ,  $\vec{P}_2$  and  $\vec{P}_3$ , respectively. This gives:

$$T = \sum_{k=1}^3 \frac{\vec{P}_k^2}{2\mu_k} \quad (9)$$

with  $\mu_k$  ( $k \in \{1, 2, 3\}$ ) being masses depending on the problem.

With our particular choice of vectors:

$$\mu_1 = m_H \quad \mu_2 = m_D \quad \mu_3 = \frac{m_H(m_H + m_O + m_D)}{2m_H + m_O + m_D} \quad (10)$$

that is, the masses associated to the Radau vectors are the masses of the ‘satellite’ atoms  $H_b$  and  $D$  of  $H_bOD$  and the one of the Jacobi vector is the reduced mass of  $H_a$  and  $H_bOD$ . The study of the  $H_a + H_bOD$  system is therefore equivalent to that of three fictive particles with these three masses, respectively. It is worth noting that, owing to the heavier mass of oxygen than those of the other atoms, these vectors can be roughly interpreted as the distance vectors from  $O$  to  $H_a/D/H_b$ , respectively. This is also the reason why this choice of vectors is suitable for the description of the exchange processes in eq. (1), since each of the regions of the configuration space corresponding to  $R_k \rightarrow +\infty$  (for  $k \in \{1, 2, 3\}$ ) describes an exchange reaction ( $k = 1$  or  $2$ ) or recoil ( $k = 3$ ). Note also that the abstraction reactions channels would correspond to regions where *pairs* of radial coordinates tend to infinity *simultaneously*.

We choose to parametrize these vectors with polyspherical coordinates, where each vector is described by spherical coordinates (one distance and two angles) with respect to a frame of reference moving with other vectors:  $\vec{R}_1$ ,  $\vec{R}_2$  and  $\vec{R}_3$  are respectively defined by the triplets of coordinates  $(R_1, \gamma_s, \theta)$ ,  $(R_2, \alpha_s, \beta_s)$  and  $(R_3, \alpha, \beta)$  (see fig. 2). By using a separation into two subsystems<sup>82</sup> with the two Radau coordinates for the water-d1 molecule,<sup>83</sup> which can be seen as a very particular case of the systematic approach of Gatti and Lung,<sup>79,84,85</sup> twice the quantized form of the kinetic energy operator of this system reads:

$$\begin{aligned} 2\hat{T} &= -\frac{\hbar^2}{\mu_3} \frac{\partial^2}{\partial R_3^2} + \frac{\hat{L}_3^\dagger \cdot \hat{L}_3}{\mu_3 R_3^2} + 2\hat{T}_{HOD} \\ &= -\frac{\hbar^2}{\mu_3} \frac{\partial^2}{\partial R_3^2} + \frac{(\hat{J} - \hat{L}_{1,2})^\dagger \cdot (\hat{J} - \hat{L}_{1,2})}{\mu_3 R_3^2} + 2\hat{T}_{HOD} \\ &= -\frac{\hbar^2}{\mu_3} \frac{\partial^2}{\partial R_3^2} + \frac{\hat{J}^\dagger \cdot \hat{J} + \hat{L}_{1,2}^\dagger \cdot \hat{L}_{1,2} - 2\hat{J}^\dagger \cdot \hat{L}_{1,2}}{\mu_3 R_3^2} + 2\hat{T}_{HOD} \\ &= -\frac{\hbar^2}{\mu_3} \frac{\partial^2}{\partial R_3^2} + \frac{\hat{J}^2 + \hat{L}_{1,2}^2 - 2\hat{J}_z^\dagger \hat{L}_{1,2} - \hat{J}_+(\hat{L}_{1,2}) - \hat{J}_-(\hat{L}_{1,2})}{\mu_3 R_3^2} + 2\hat{T}_{HOD} \end{aligned} \quad (11)$$

where  $\dagger$  denotes the Hermitian conjugate of the operator, which appears here since we work with conjugate momenta of curvilinear coordinates (see e.g. refs. 86–88). Here  $\hat{T}_{HOD}$  is the kinetic energy of HOD in the space-fixed frame of reference:

$$\begin{aligned}
2\hat{T}_{\text{HOD}} = & -\frac{\hbar^2}{\mu_1} \frac{\partial^2}{\partial R_1^2} - \frac{\hbar^2}{\mu_2} \frac{\partial^2}{\partial R_2^2} + \hbar^2 \left( \frac{1}{\mu_1 R_1^2} + \frac{1}{\mu_2 R_2^2} \right) \left( \frac{\partial}{\partial u} (1-u^2) \frac{\partial}{\partial u} + \frac{1}{1-u^2} \frac{\partial^2}{\partial \gamma_s^2} \right) \\
& + \frac{1}{\mu_2 R_2^2} \left[ \hat{L}_{1,2}^2 - 2(\hat{L}_{1,2})_z^2 + \hbar \left( -\sqrt{1-u^2} \frac{\partial}{\partial u} + \frac{1}{2} \frac{u}{\sqrt{1-u^2}} \right) \left( (\hat{L}_{1,2})_+^{\text{BFs}} - (\hat{L}_{1,2})_-^{\text{BFs}} \right) \right. \\
& \left. + \frac{u}{2\sqrt{1-u^2}} \left( (\hat{L}_{1,2})_+^{\text{BFs}} (\hat{L}_{1,2})_z^{\text{BFs}} + (\hat{L}_{1,2})_-^{\text{BFs}} (\hat{L}_{1,2})_z^{\text{BFs}} \right. \right. \\
& \left. \left. + (\hat{L}_{1,2})_z^{\text{BFs}} (\hat{L}_{1,2})_+^{\text{BFs}} + (\hat{L}_{1,2})_z^{\text{BFs}} (\hat{L}_{1,2})_-^{\text{BFs}} \right) \right]
\end{aligned} \tag{12}$$

where we have carried out a change of variable  $u = \cos \theta$ . In eq. (11),  $\hat{J}$  and  $\hat{L}_{1,2} = \hat{L}_1 + \hat{L}_2$  are respectively vector operators of the total angular momentum and the angular momentum of  $\text{H}_b\text{OD}$  (corresponding to the fictive particles 1 and 2 together).  $\hat{J}^2$ ,  $\hat{J}_z$  and  $\hat{J}_\pm$  are the magnitude squared, the  $z$ -component and the ladder operators of the angular momentum of  $\text{H}_a\text{H}_b\text{OD}$ .  $\hat{L}_{1,2}^2$  and  $(\hat{L}_{1,2})_z$  are the magnitude squared and the  $z$ -component of  $\hat{L}_{1,2}$  in the space-fixed frame of reference. In eq. (12), the operators  $(\hat{L}_{1,2})_+^{\text{BFs}}$ ,  $(\hat{L}_{1,2})_-^{\text{BFs}}$  and  $(\hat{L}_{1,2})_z^{\text{BFs}}$  are the lowering, raising and  $z$ -component of the angular momentum  $\hat{L}_{1,2}$  projected on the (BFs) frame of reference axes (still expressed within the space-fixed frame of reference).

The kinetic energy operator  $\hat{T}$ , written as in eqs. (11) and (12), can be implemented in the Heidelberg MCTDH package which will be introduced in section 5. The correctness of the operator  $\hat{T}_{\text{HOD}}$  and its implementation have been tested numerically as explained in appendix B.

## 4 Definition of the initial state

As our main focus is on the collision between  $\text{H}_a$  and  $\text{H}_b\text{OD}$ , the wavefunction  $\Psi$  of the system  $\text{H}_a\text{H}_b\text{OD}$  will be a function of the internal coordinates  $R_1, R_2, R_3, \beta_s, \gamma_s$  and  $u$  as well as the external angle  $\alpha_s$ . For a fixed orientation ( $\alpha, \beta, \gamma = \alpha_s$ ), there is a one-to-one relation between these internal coordinates and the space-fixed Cartesian coordinates  $\vec{x}_{\text{H}_a}, \vec{x}_{\text{H}_b}, \vec{x}_{\text{D}}, \vec{x}_{\text{O}}$  of the atoms in  $\text{H}_a + \text{H}_b\text{OD}$ . The definition of the initial state  $\Psi_0$  of the system  $\text{H}_a + \text{H}_b\text{OD}$  is specified by invoking the Franck-Condon approximation: the excitation is so fast that the complex retains its geometry, given by its (ro-)vibrational ground state  $\psi_g$ , as it transits to the electronic excited state. Moreover, the hydrogen-bond is disregarded in the photodissociation process of  $\text{H}_a\text{Cl}$ , as the intermolecular binding energy is small with respect to the excess energy  $\Delta V_{\text{exc}}$ .

This allows to consider that (a) the potential energy curves of the  $X^1\Sigma$  and  $A^1\Pi$  states of  $\text{H}_a\text{Cl}$  remain the same as when it is isolated and (b) the centers of masses of  $\text{H}_a\text{Cl}$  and  $\text{H}_b\text{OD}$  keep the same distance at all times. Now, as we will be observing the collision occurring between  $\text{H}_a$  and  $\text{H}_b\text{OD}$  in the space-fixed frame of these four atoms (and not the frame of the whole complex, which includes Cl), we must correct the partial momentum of the released hydrogen atom. The relative momentum between  $\text{H}_a$  and

$\text{H}_b\text{OD}$  becomes:

$$p'_{\text{exc}} = \left( 1 - \frac{m_{\text{H}}}{2m_{\text{H}} + m_{\text{D}} + m_{\text{O}}} \right) p_{\text{exc}} \tag{13}$$

as shown in appendix A. The classical translational kinetic energy of collision is then, in the frame of reference of  $\text{H}_a + \text{H}_b\text{OD}$ ,  $E_{\text{coll}} = \Delta V_{\text{exc}}(m_{\text{Cl}}/m_{\text{HCl}})(m_{\text{HOD}}/m_{\text{H}_2\text{OD}}) = 3.03$  eV.

In view of these assumptions, the initial state of the propagation is defined in the rotational ground state  $J = 0$  as:

$$\Psi_0(R_1, R_2, R_3, u, \alpha_s, \beta_s, \gamma_s) = \psi_g(R_1, R_2, R_3, u, \beta_s, \gamma_s) e^{-ip'_{\text{exc}} R_3 / \hbar} \tag{14}$$

Equation (14) expresses the fact that the momentum of the so-defined wavepacket is that given by full photodissociation of  $\text{H}_a\text{Cl}$ . Although  $\text{H}_a$  is not fully dissociated from Cl when the former reaches  $\text{H}_b\text{OD}$ , it is shown in appendix C that this aspect has not a major impact on the outcome of the propagation. Note also that, since the atoms Cl,  $\text{H}_a$  and O in the complex are aligned and  $G$  almost coincides with oxygen, we consider that the momentum of  $\text{H}_a$  is entirely converted into momentum along the  $R_3$  coordinate.

## 5 Computational details

This study has been carried out with the Multi-Configuration Time-Dependent Hartree method (MCTDH),<sup>89-93</sup> more precisely the Heidelberg MCTDH package (version 8.5.11).<sup>94</sup> The wavefunction  $\Psi$  to be propagated is defined over a grid in the internal coordinates  $R_1, R_2, R_3, \beta_s, \gamma_s$  and  $u$  plus the overall rotation angle  $\gamma = \alpha_s$ . The chosen wavefunction ansatz is:

$$\begin{aligned}
\Psi(R_1, R_2, R_3, u, \alpha_s, \beta_s, \gamma_s, t) \\
= \sum_{i_1=0}^{n_1} \sum_{i_2=0}^{n_2} \sum_{i_3=0}^{n_3} A_{i_1, i_2, i_3}(t) \varphi_{i_1}^{(1)}(R_1, u, t) \varphi_{i_2}^{(2)}(R_2, R_3, t) \\
\times \varphi_{i_3}^{(3)}(\alpha_s, \beta_s, \gamma_s, t)
\end{aligned} \tag{15}$$

That is, we use three sets of combined-modes single-particle functions (SPF). The SPFs are defined, for  $i_1 \in \{1, \dots, n_1\}$ ,  $i_2 \in \{1, \dots, n_2\}$  and  $i_3 \in \{1, \dots, n_3\}$ , as:

$$\varphi_{i_1}^{(1)}(R_1, u, t) = \sum_{j_1=0}^{N_{1,1}} \sum_{j_2=0}^{N_{1,2}} c_{i_1, j_1, j_2}^{(1)}(t) \chi_{j_1}^{(1,1)}(R_1) \chi_{j_2}^{(1,2)}(u) \tag{16}$$

Table 1 Definition of the grid and of the corresponding primitive basis.

$\kappa$	Coord.	PBF type <sup>1</sup>	$N_\kappa$	Range	Units <sup>2</sup>	$n_i$
(1, 1)	$R_1$	sin	30	[1.0, 5.0]	$a_0$	20
(1, 2)	$u$	sin	20	[-0.99, 0.6]	–	–
(2, 1)	$R_2$	sin	40	[1.0, 5.0]	$a_0$	25
(2, 2)	$R_3$	sin	55	[1.0, 7.0]	$a_0$	–
(3, 1)	$\alpha_s$	k	1	–	–	16
(3, 2)	$\beta_s$	wigner	20	–	–	–
(3, 3)	$\gamma_s$	exp	31	[0, 2 $\pi$ ]	rad	–

<sup>1</sup> sin = particle in a box eigenfunctions ; wigner = Wigner rotation matrix elements ; exp = imaginary exponentials with periodic boundary conditions ; k =  $K$ -rotational quantum number in the Wigner-DVR

<sup>2</sup> 1  $a_0 = 1$  Bohr = 0.529 Å

$$\varphi_{i_2}^{(2)}(R_2, R_3, t) = \sum_{j_1=0}^{N_{2,1}} \sum_{j_2=0}^{N_{2,2}} c_{i_2, j_1, j_2}^{(2)}(t) \chi_{j_1}^{(2,1)}(R_2) \chi_{j_2}^{(2,2)}(R_3) \quad (17)$$

and

$$\varphi_{i_3}^{(3)}(\alpha_s, \beta_s, \gamma_s, t) = \sum_{j=0}^{N_{3,1}} \sum_{k=0}^{N_{3,2}} \sum_{m=0}^{N_{3,3}} c_{i_3, j, k, m}^{(3)}(t) \chi_{j, k, m}^{(3)}(\alpha_s, \beta_s, \gamma_s) \quad (18)$$

The functions  $\chi_j^{(\kappa)}(q_\kappa)$  – where  $\kappa$  is a multi-index labelling a coordinate in a mode, e.g.  $\kappa = (2, 1)$  labels the coordinate  $R_2$  – are the time-independent primitive basis functions (PBF). These functions, for the coordinates  $R_1$ ,  $R_2$ ,  $R_3$  and  $u$ , are chosen to be the discrete variable representation (DVR) associated with particle-in-a-box eigenfunctions:

$$\chi_j^\kappa(q_\kappa) = \sqrt{\frac{2}{L_\kappa}} \sin\left(\frac{\pi j(q_\kappa - q_\kappa^{\min})}{L_\kappa}\right) \quad (19)$$

where the coordinate  $q_\kappa$  takes values between  $q_\kappa^{\min}$  and  $q_\kappa^{\max}$ , and  $L_\kappa = q_\kappa^{\max} - q_\kappa^{\min}$ . For the angular coordinates we choose the DVR associated with an expansion in Wigner rotation matrix elements which are non-direct product functions of the three angles:

$$\chi_{j, k, m}^{(3)}(\alpha_s, \beta_s, \gamma_s) = \sqrt{\frac{2(j+1)}{8\pi^2}} D_{m, k}^j(\alpha_s, \beta_s, \gamma_s) \quad (20)$$

where

$$D_{m, k}^j(\alpha_s, \beta_s, \gamma_s) = e^{-im\gamma_s/\hbar} d_{m, k}^j(\cos\beta_s) e^{-ik\alpha_s/\hbar} \quad (21)$$

the functions  $d_{m, k}^j$  are Jacobi polynomials.<sup>95</sup>

The discrete points where the wavefunction and the potential energy operators are evaluated in coordinate space are determined by the DVR algorithm built into the MCTDH program. These correspond to Gaussian quadrature points specific to the type of PBF used for each degree of freedom. The number of grid points  $N_\kappa$  along a given coordinate equals the number of primitive functions used in the expansions in eqs. (16) to (18). The parameters of the grid/PBF expansions are given in table 1.

The ground state wavefunction  $\psi_g$  of the complex

( $H_aCl$ )...( $H_bOD$ ) was obtained by improved relaxation<sup>96</sup> on the potential energy surface by Mancini and Bowman<sup>73</sup> with implicit inclusion of the Cl atom. By ‘‘implicit’’ we mean that the position of the Cl atom is deduced by the position of the other ones  $H_a$ ,  $H_b$ , D and O. To be specific, the potential energy function  $V$  used in this relaxation is a function of the coordinates  $\vec{x}_{H_a}$ ,  $\vec{x}_{H_b}$ ,  $\vec{x}_D$ ,  $\vec{x}_O$  (or, equivalently, as a function of the internal coordinates, since the potential is invariant by overall rotation and translation) and its definition is related to the original potential energy surface of the complex  $U$  by:

$$V(\vec{x}_{H_a}, \vec{x}_{H_b}, \vec{x}_D, \vec{x}_O) = U(\vec{x}_{H_a}, \vec{x}_{H_b}, \vec{x}_D, \vec{x}_O, \underbrace{f(\vec{x}_{H_a}, \vec{x}_O)}_{=\vec{x}_{Cl}}) \quad (22)$$

with  $f$  defined as

$$f(\vec{x}_{H_a}, \vec{x}_O) = \vec{x}_{H_a} + \frac{\vec{x}_{H_a} - \vec{x}_O}{\|\vec{x}_{H_a} - \vec{x}_O\|} R_e \quad (23)$$

In other words, the chlorine atom is placed along the ( $OH_a$ ) axis, behind the hydrogen atom at a fixed distance  $R_e = 1.29$  Å corresponding to the equilibrium bond length of HCl in the ( $HCl$ )...( $H_2O$ ) complex at the  $C_s$  geometry. The kinetic energy operator used for the relaxation is the one in eq. (11), thus missing some terms related to the HCl elongation and rotation which are neglected. However, this procedure still allows to obtain a physically reasonable ground state wavefunction  $\psi_g$  without explicit consideration of the Cl coordinates which are not of interest in the subsequent collision between  $H_a$  and  $H_bOD$ . We could indeed obtain a wavefunction with  $C_{2v}$  symmetry, with expectation values of the coordinates in agreement with the ground state geometry found by Mancini and Bowman. The potential was reconstructed as a sum of products of ‘one particle’ (also called ‘natural’) potentials – a suitable form for the evaluation of its action on the MCTDH ansatz (eq. (15)) – with the POTFIT program.<sup>97–99</sup> A narrow relevant region including the double-well potential was considered for the fit. Contraction along the mode ( $R_2, R_3$ ) was performed whereas, for the modes ( $R_1, u$ ) and ( $\beta_s, \gamma_s$ ), 213 and 166 natural potentials were respectively included for the fit and, after a few fitting iterations, the rms error in the relevant regions was 20.7 meV.

The wavefunction  $\psi_g$  obtained above is then multiplied by the imaginary exponential as in eq. (14) so as to obtain the initial state for the subsequent dynamics of the  $H_a + H_bOD$  collision, for which we used the  $H_3O$  potential energy surface of Chen *et al.*<sup>100</sup> (of the three versions presented in the paper, the NN1 was chosen). The latter was POTFITted over a region corresponding to energies below 6.1 eV (the reference being at the  $H + H_2O$  asymptote). The mode ( $R_2, R_3$ ) was again contracted and, for the other modes, we used 191 and 77 natural potentials for the fit. The obtained rms error in the relevant region was, after several iterations, 14.3 meV.

Additional complex absorbing potentials (CAPs) were added at the ends of the three reaction channels in which the wavefunction had more likelihood to exit: the  $H_aOD + H_b$  and  $H_aHO_b + D$  exchange channels (which we label ‘1’ and ‘2’, respectively) and the  $H_a + H_bOD$  recoil channel (‘3’). In practice, the CAPs were

placed at the ends of the grid for large values of  $R_1$ ,  $R_2$  and  $R_3$  and were of the form (for  $k \in \{1, 2, 3\}$ ):

$$\Theta_k(R_k) = -i\eta_k \cdot \Gamma(R_k - R_k^0) \cdot (R_k - R_k^0)^2 \quad (24)$$

where  $\Gamma$  is the Heaviside step function,  $R_k^0$  is the starting point of the  $k^{\text{th}}$  CAP and  $\eta_k$  its strength. The lengths (i.e.  $\max(R_k) - R_k^0$ ) of the CAPs were set to  $1.5 a_0$  at the ends of channels ‘1’ and ‘2’ and to  $2 a_0$  for channel ‘3’. The strengths were chosen by an automated optimization procedure – included in the MCTDH package – in order to minimize the reflection on and transmission through these.<sup>101–103</sup> Due to the limited range of values taken by  $R_3$  and the fact that the initial state is located in the region covered by the third CAP, the latter was activated only a few femtoseconds after the beginning of the propagation, i.e. when the wavepacket would mostly be outside that region.

Time-resolved reaction probabilities  $P_k(t)$  with  $k \in \{1, 2, 3\}$  for the three outcomes listed above (two exchanges and one recoil) were calculated by accumulation in time of the probability current along each of the three channels. The latter were evaluated by taking the expectation value of the flux operators  $\hat{F}_k$  defined as the following commutator<sup>104</sup> (for  $k \in \{1, 2, 3\}$ ):

$$\hat{F}_k = [\hat{H}, \Gamma(R_k - R_k^0)] = [\hat{T}, \Gamma(R_k - d)] \quad (25)$$

with  $\hat{H} = \hat{T} + \hat{V}_{\text{H} + \text{H}_2\text{O}}$  and  $d = 3.5 a_0$ . In the following we call ‘interaction region’ the portion of the configuration space where, for  $k \in \{1, 2, 3\}$ ,  $0 < R_k < d$ . The reaction probability in each channel  $k$  is then given by:

$$P_k(t) = \int_0^t \langle \Psi(\tau) | \hat{F}_k | \Psi(\tau) \rangle d\tau + P_k(0) \quad (26)$$

where  $P_k(0)$  is the probability of finding the system in the region where  $R_k < d$  at  $t = 0$ .

In addition, energy-resolved reactions probabilities along the three channels were calculated too. The computation of these quantities depend on the energy distribution  $\Delta(E)$  of the wavefunction which is determined by the (inverse) energy-time Fourier transform of the wavefunction autocorrelation function:

$$\begin{aligned} \Delta(E) &= \frac{1}{2\pi\hbar} \int_{-\infty}^{+\infty} \langle \Psi(0) | \Psi(\tau) \rangle e^{iE\tau/\hbar} d\tau \\ &= \frac{1}{\pi\hbar} \text{Re} \left( \int_0^T \langle \Psi(0) | \Psi(\tau) \rangle e^{iE\tau/\hbar} d\tau \right) \end{aligned} \quad (27)$$

where  $T$  is the final time of the propagation. In the following, we will represent energy-dependent quantities as functions of the collision energy between  $\text{H}_a$  and  $\text{H}_b\text{OD}$ . The energy axes are thus shifted by  $0.498389$  eV corresponding to the vibrational zero-point energy of the latter. This energy is calculated by improved relaxation of  $\text{H}_b\text{OD}$  on the same surface we use for the dynamics (where  $\text{H}_a$  is fixed, far away from  $\text{H}_b\text{OD}$ , see appendix B for details). In order to calculate the reaction probabilities, one needs the energy-dependent fluxes  $\phi_k(E)$  for  $k \in \{1, 2, 3\}$  at the end of each channel. These can be computed thanks to the CAPs:<sup>92,93</sup>

$$\phi_k(E) = \frac{2}{\pi\hbar} \text{Re} \left( \int_0^T g_k(\tau) e^{iE\tau/\hbar} d\tau \right) \quad (28)$$

with:

$$\begin{aligned} g_k(\tau) &= \int_0^{T-\tau} \langle \Psi(t) | \Theta_k | \Psi(t+\tau) \rangle d\tau \\ &\quad + \frac{1}{2} \langle \Psi(T-\tau) | \Gamma(R_k - R_k^0) | \Psi(T) \rangle \end{aligned} \quad (29)$$

Eventually, the energy-resolved reaction probabilities are given by:

$$\Pi_k(E) = \frac{\phi_k(E)}{\Delta(E)} \quad (30)$$

Because of the presence of CAPs, the norm of the wavefunction would eventually decrease during the propagation. We let it proceed until the former would fall below  $10^{-3}$ , for which a propagation time of 130 fs is sufficient.

The convergence of our results was checked by inspection of (1) the squares of absolute values of the expansion coefficients  $c_{i,j,k,m}^{(\kappa)}(t)$  and the populations at the ends of the grid and (2) the magnitude of the natural weights (i.e. the eigenvalues of the one-mode density matrices  $\sum_{i\kappa} |\varphi_{i\kappa}^{(\kappa)}\rangle \langle \varphi_{i\kappa}^{(\kappa)}|$ ). It was required that, over the entire propagation, the smallest value of each of the quantities in (1) and (2) was below  $10^{-3}$  and  $10^{-4}$ , respectively. In addition, we required that the sum of the energy-resolved reaction probabilities would be as close as possible to unity within a 1% error over the largest possible collision energy range. The precision constraint was satisfied by further increasing the number of SPF. The coverage of a larger portion of the energy spectrum was made possible by carrying out additional propagations at slightly higher or lower collision energy (namely by increasing or decreasing  $p'_{\text{exc}}$  – we chose 16 a.u. and 22 a.u., respectively) and then joining the respective calculated reaction probabilities  $\Pi_i^{\oplus}$  and  $\Pi_i^{\ominus}$  to the main one  $\Pi_i^0$  by using smooth switching sigmoid-type functions:

$$\begin{aligned} \Pi_i(E) &= \Pi_i^{\ominus}(E)(1 - s(E - \varepsilon_{\ominus}))(1 - s(E - \varepsilon_{\oplus})) \\ &\quad + \Pi_i^0(E)s(E - \varepsilon_{\ominus})(1 - s(E - \varepsilon_{\oplus})) \\ &\quad + \Pi_i^{\oplus}(E)s(E - \varepsilon_{\ominus})s(E - \varepsilon_{\oplus}) \end{aligned} \quad (31)$$

where  $s(E) = (1 + \exp(-E/\varepsilon))^{-1}$ , the junction extent is  $\varepsilon = 0.1$  and the junction points are  $(\varepsilon_{\ominus}, \varepsilon_{\oplus}) = (2.5, 4.1)$  eV.

The chosen parameters to achieve the desired level of precision are the ones given in table 1.

## 6 Results and discussion

### 6.1 Main results

We first look at the evolution of the nuclear wavepacket over time. The most relevant coordinates for tracking the present process in eq. (1) are the radial ones  $R_1$ ,  $R_2$  and  $R_3$  (since, as noted in section 3, they roughly correspond to the O–H<sub>b</sub>, O–D and O–H<sub>a</sub> bond distances, respectively). Figure 3 displays three contour plots of cuts of the potential energy surface of  $\text{H}_3\text{O}$  as functions of different pairs of these coordinates. In these cuts, the angular coordinates  $u$ ,  $\beta_s$  and  $\gamma_s$  as well as, in turns,  $R_1$ ,  $R_2$  or  $R_3$ , were chosen as their respective expectation value at  $t = 0$ . On top of the PES cuts, the marginal probability densities (also known as

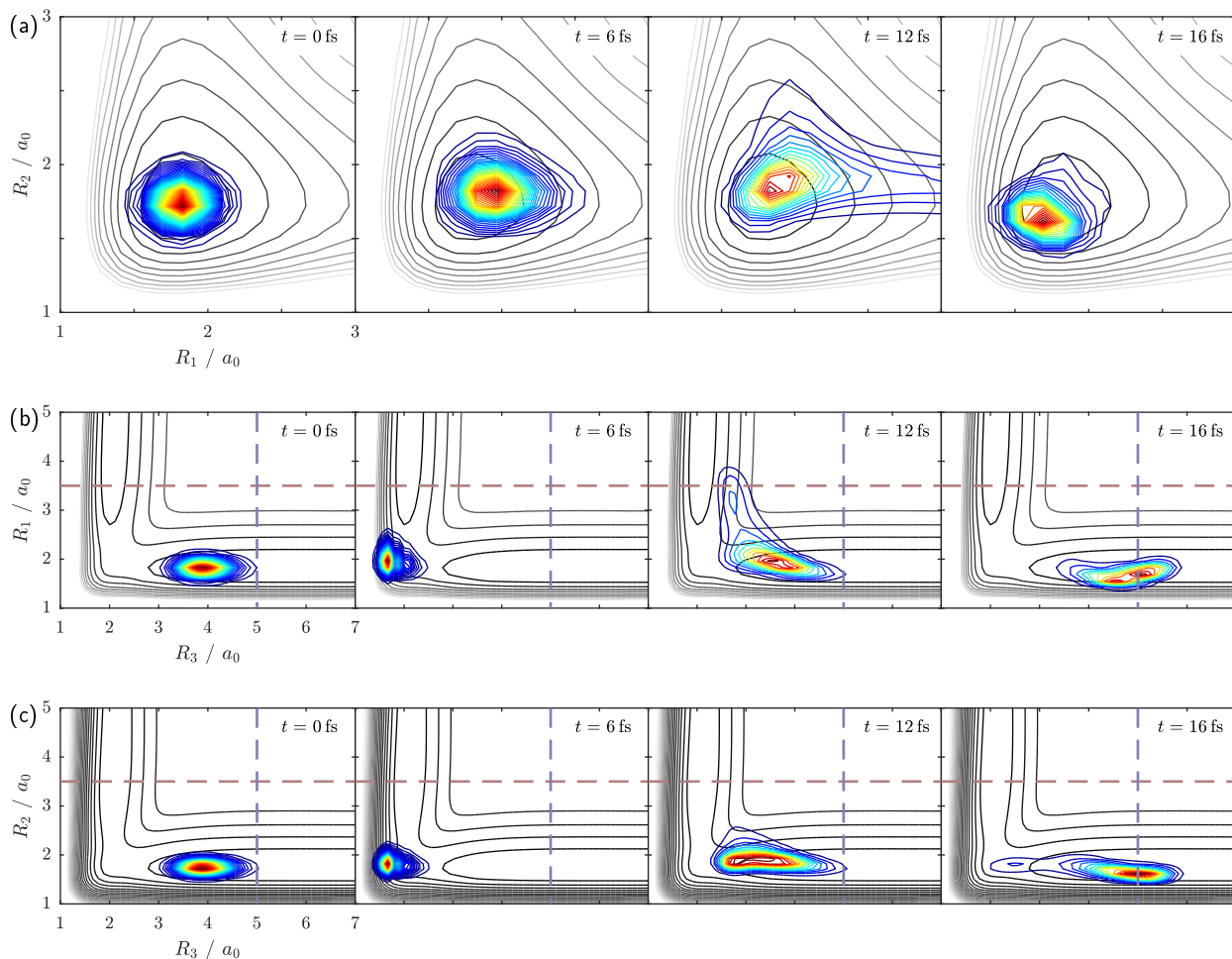


Fig. 3 Snapshots of the reduced densities (coloured contours) of the wavepacket as functions of different pairs of radial coordinates: (a)  $R_1$  and  $R_2$ , (b)  $R_3$  and  $R_1$  and (c)  $R_3$  and  $R_2$ . These are overlaid over cuts of the PES (grey-scaled contours) where the fixed coordinates equal their expectation value in the initial state. The dashed lines denote the beginning of a complex absorbing potential.

‘reduced densities’) are represented at different times during the propagation. These were evaluated by integrating  $|\Psi(t)|^2$  with respect to all but two radial coordinates over the entire grid.

The marginal probabilities are, at  $t = 0$ , Gaussian-like functions of the radial coordinates located around  $\langle R_1 \rangle = 1.81 a_0$ ,  $\langle R_2 \rangle = 1.78 a_0$  and  $\langle R_3 \rangle = 4.0 a_0$ . This reflects the fact that the initial state describes the  $H_a$  atom and the  $H_bOD$  molecule as separated bodies. Note, though, that the wavepacket is not infinitely far from the interaction region: it is indeed lying on the uphill slope of the PES (see e.g. fig. 16) leading to the  $H_aH_bDO$  transient (a saddle point  $[H_a(H_bOD)]^\ddagger$  and a shallow local minimum  $H_aH_bOD$  behind it). As time unfolds, because of the initial momentum  $-p'_{exc}$  in the direction of  $\vec{R}_3$ , the wavepacket approaches the interaction region. As shown in figs. 3b and 3c, it quickly reaches  $\langle R_3 \rangle \approx 1.6 a_0$ , crossing many high-lying contour lines of the repulsive potential wall, yet keeping the  $H_bOD$  molecule undisturbed (see fig. 3a). Around 12 fs, the wavepacket is almost entirely rejected back towards large values of  $R_3$ , i.e. in the non-reactive scattering channel ‘3’. There is just a small fraction of the wavepacket that stands out and manages to enter the reactive channel ‘1’ corresponding to the  $H_a/H_b$  exchange (see

figs. 3a and 3b at 12 fs). During this time, no O–D dissociation seems to be observable (fig. 3c). The abstraction reactions are also totally absent.

Since this collision unfolds over a few femtoseconds, the chlorine atom must have not moved a lot from its original position because of its large mass relative to that of  $H_a$  (we estimate that in 10 fs the Cl atom moves only by 0.07 Å). This raises the question whether the rejected  $H_a$  atom meets Cl again, causing multiple collisions of  $H_a$  against  $H_bOD$ .

Investigation of the motion of the wavepacket over time in the coordinates  $\beta_s$  (which roughly corresponds to the angle  $\widehat{H_aOD}$ ) and  $\gamma_s$  (which is approximately  $\pi$  minus the dihedral angle between O– $H_a$  and O– $H_b$  about the OD axis) suggests an answer. As shown in fig. 4, the wavepacket does not move much until the collision between  $H_a$  and O occurs, at  $t = 6$  fs. The peak of the reduced density then quickly moves to larger values of  $|\gamma_s|$ . This is accompanied by a slight shift towards smaller  $\beta_s$ . By looking at the propagation in the coordinates  $R_3$  and  $\gamma_s$ , shown in fig. 5, one sees again that the displacement of the wavepacket from  $\gamma_s = 0$  to  $|\gamma_s| > 0$  happens after the collision at  $t = 6$  fs. On the rightmost panel at  $t = 16$  fs, it can be seen that the part of

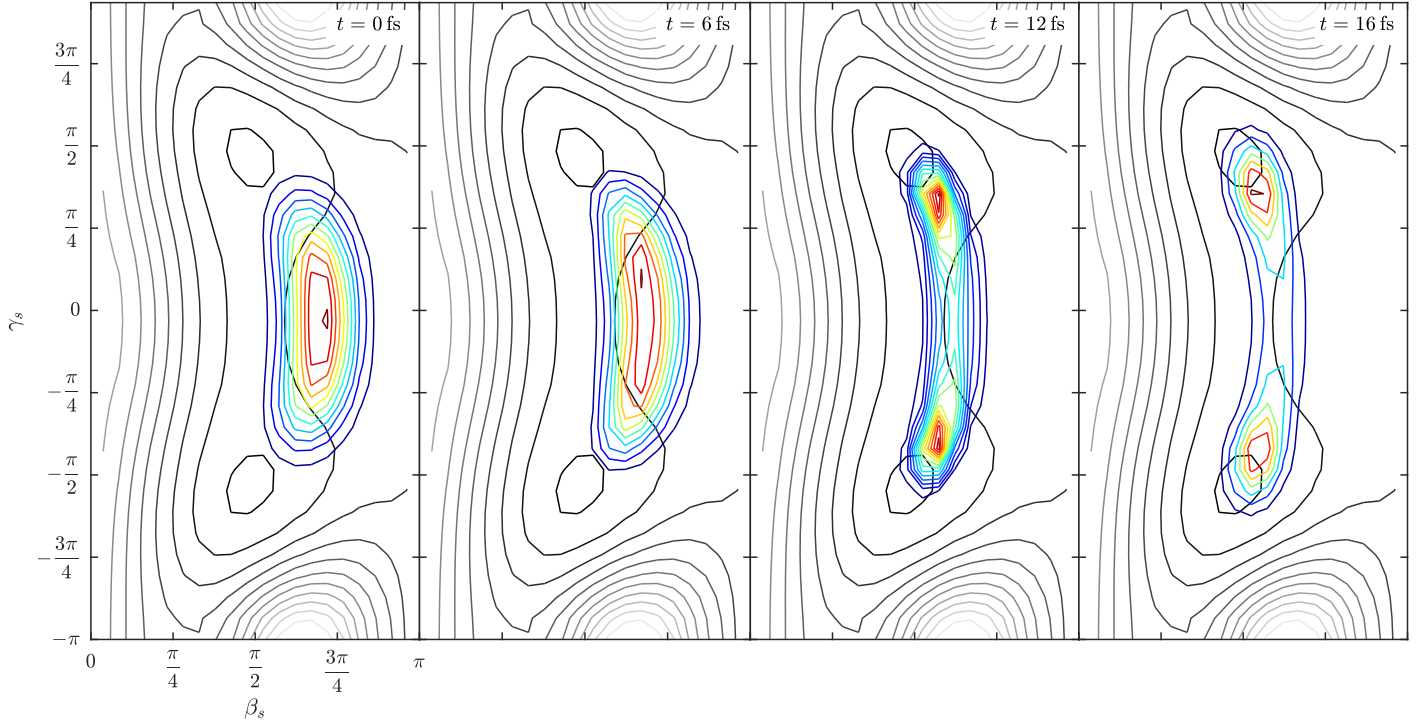


Fig. 4 Reduced density (coloured contour lines) of the wavepacket of the main propagation as a function of the angular coordinates  $\beta_s$  and  $\gamma_s$  at different times. The black contour lines correspond to the cut of the potential energy surface at the expectation values of the other coordinates at  $t = 0$ .

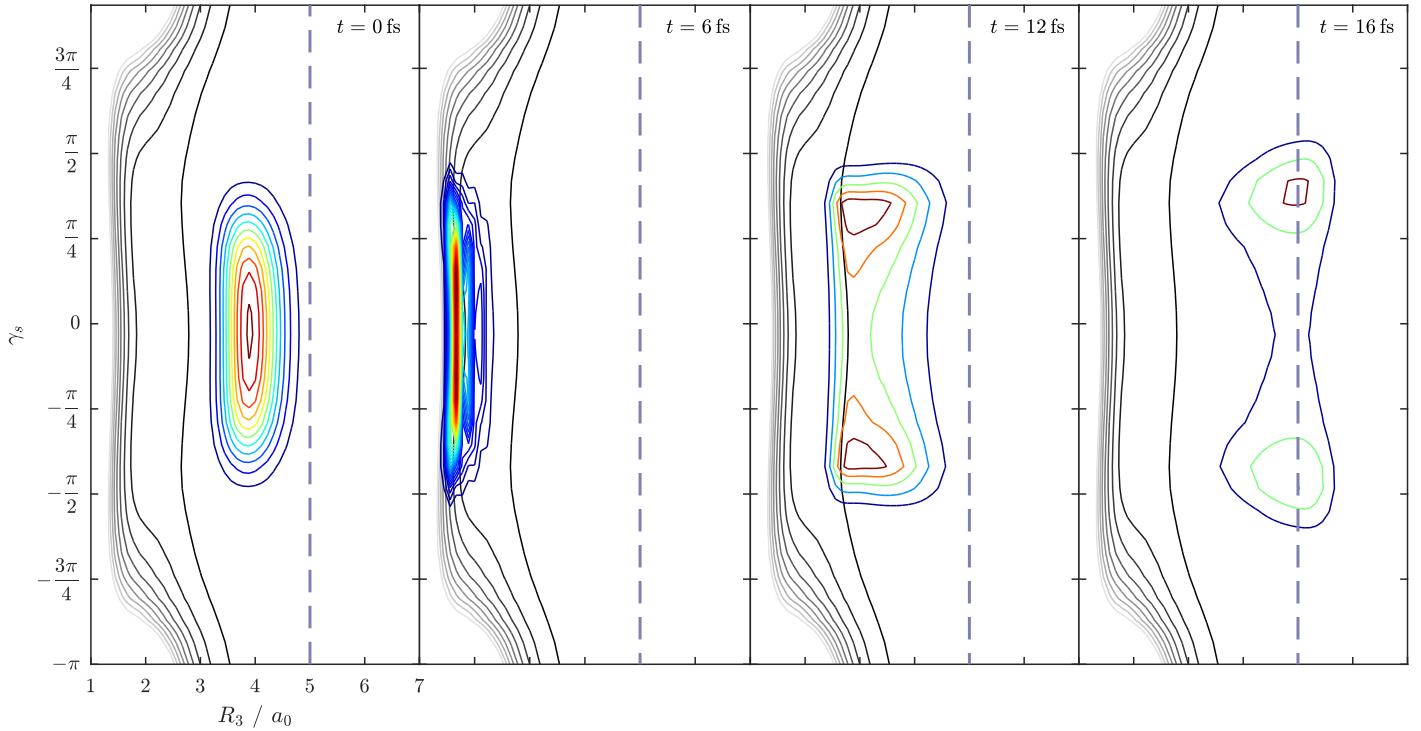


Fig. 5 Reduced density (coloured contour lines) of the wavepacket of the main propagation as a function of the coordinates  $R_3$  and  $\gamma_s$  at different times. The black contour lines correspond to the cut of the potential energy surface at the expectation values of the other coordinates at  $t = 0$ . The dashed line indicates the beginning of the complex absorbing potential.

the wavefunction describing the return to increasing values of  $R_3$  is mostly away from the plane  $\gamma_s = 0$ . This splitting of the wavepacket can be explained by the fact that, on its way to the  $H_a + H_bOD$  collision, it is propagating along a barrier that separates the local minima of  $H_2DO$  (which, with only regular hydrogen, correspond to the  $C_{3v}$  geometries of  $H_3O$ ,<sup>100,108</sup> each being a mirror image of the other). That barrier has a height of about  $1200\text{ cm}^{-1}$ , i.e. much higher than that separating the  $C_{2v}$  minima of  $(HCl)\cdots(HOD)$  ( $59\text{ cm}^{-1}$ ).<sup>73</sup> Thus, in contrast with the situation of  $(HCl)\cdots(HOD)$  described in section 2, the wavepacket separates into two distinct ones.

As a result, a large part of the wavepacket associated to non-reactive scattering does not revisit the same region of the configuration space covered by the initial state: for the most, the angle between the  $OH_a$  axis and the  $H_bOD$  plane is different between before and after the collision. However, since the coordinates  $\beta_s$  and  $\gamma_s$  are relative coordinates describing the geometry of  $H_aH_bOD$ , they do not tell anything about its orientation with respect to the stationary Cl atom. In other words, the limit cases described by the non-reactive part of this wavepacket are (i) backscattering of  $H_a$  away from the Cl-O axis, while  $H_bOD$  retains its original orientation with respect to Cl, or (ii) rotation of  $H_bOD$  away from the initial plane of the complex, while  $H_a$  is backscattered in the direction it came from – thus still leading to backscattering of  $H_a$  against Cl and to multiple  $H_a + H_bOD$  collisions. Given that rotational motion of small molecules takes usually place on time-scales of picoseconds, this second option seems to us the least probable. As a matter of fact, the rotational constant of water with respect to the second largest principal axis (which is approximately the axis the  $H_bOD$  molecule is rotating about in the present situation) is  $\bar{B} = 14.5\text{ cm}^{-1}$ , which roughly corresponds to a rotational period of  $T = 1/2\bar{B}c = 1.15\text{ ps}$ . For the rest of this subsection, we will assume that case (i) above is what happens. The contribution of multiple collisions – case (ii) – to the overall dynamics is discussed in section 6.4.

The computation of time-resolved fluxes through delimiting surfaces in the three channels gives a more quantitative description of the process. The time evolution of the expectation value of the flux operators in eq. (25) are shown in fig. 6a. The negative flux across the delimiting surface at  $R_3 = d = 3.5 a_0$  observed at early times is due to the approaching of  $H_a$  to the  $H_bOD$  molecule: the wavefunction is flowing inside the interaction region. Shortly after, the flux across that same surface and the one placed at the O- $H_b$  dissociation channel sharply peak to positive values and simultaneously with a 4 : 1 ratio. It is only 3 to 4 fs later that the flux in the O-D dissociation channel starts increasing moderately, followed by a slow decay (see inset in the figure).

These fluxes show that the non-reactive scattering is the most probable outcome of the collision, followed by  $H_a/H_b$  exchange, and very little  $H_a/D$  exchange is observable. This is made clear by integrating the fluxes as in eq. (26). These integrals are shown in fig. 6b (the negative of the integral of  $F_3$  over the entrance phase was taken as  $P_3(t=0)$ ). After the delay time needed for  $H_a$  to reach the collision partner, the reaction probabilities  $P_1$  and  $P_3$  steeply increase : the probability of finding the system in the non-reactive scattering channel goes from almost zero to 90% of

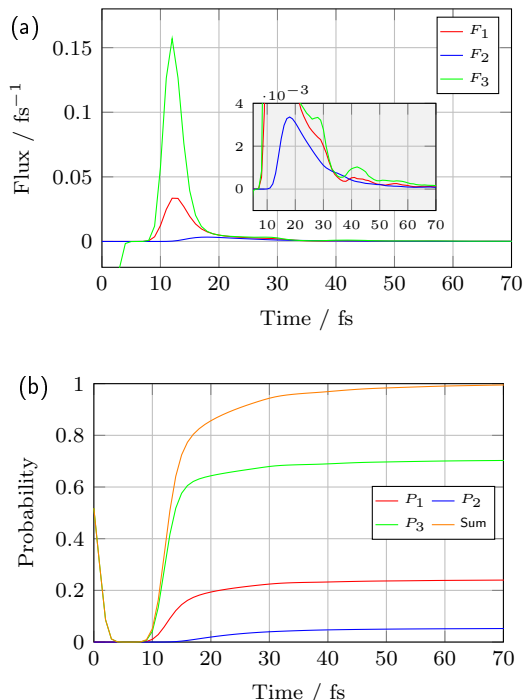


Fig. 6 Time-resolved (a) fluxes through the dividing surfaces at  $R_k = d = 3.5 a_0$  and (b) corresponding reaction probabilities as defined in eq. (26), with  $H_bOD$  initially in its vibrational ground state.

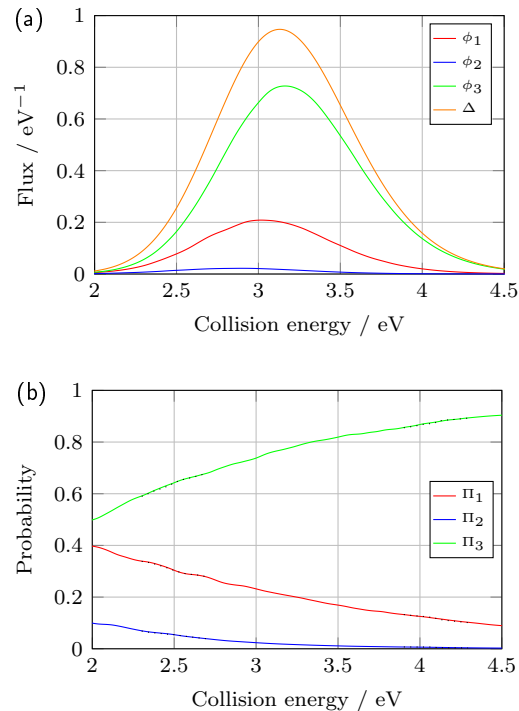


Fig. 7 Energy-resolved (a) fluxes and wavepacket energy distribution  $\Delta$  and (b) reaction probabilities. The dotted lines represent the original data around the junction points which has been smoothed with switching functions.

its maximal value in the timespan between  $t = 9$  fs and  $t = 15$  fs. The rising of the probability of  $H_a/H_b$  exchange increases in the same fashion. Instead, the probability of  $H_a/D$  exchange  $P_2$  starts increasing at slightly later moment and is slower than the others: the increase to 90% of its asymptotic value occurs in the timespan between  $t = 11$  fs to  $t = 38$  fs. As time tends to infinity, the total reaction probabilities reach  $P_1 = 24.1\%$ ,  $P_2 = 5.4\%$  and  $P_3 = 70.5\%$ .

An insight on the contributions of the different energy components of the wavepacket to this process can be obtained by the evaluation of the energy-resolved fluxes at the end of each reaction channel. These and the wavepacket energy distribution  $\Delta(E)$  are shown in fig. 7a. As anticipated, the energy distribution of the wavepacket is a broad Gaussian-like function centered at 3.1 eV. The fluxes evaluated at the ends of the three channels are also smooth, bell-shaped functions of the collision energy, each having its maximum at a slightly higher or lower value. It can again clearly be seen from the values taken by  $\phi_3$  that the most probable outcome of the collision is the non-reactive scattering of  $H_a$  by  $H_bOD$ . On the other hand, within the fraction of successful exchange reactions, the one involving the dissociation of the O– $H_b$  bond with subsequent departure of  $H_b$  is the most favoured and very little dissociation of the O–D bond would be observed.

A clearer comparison of these fluxes can be discussed by computing the energy-resolved reaction probabilities as in eq. (30). These are shown in fig. 7b. We see, as in the time-dependent picture, that the non-reactive scattering is the most prominent outcome. This becomes more and more the case as the collision energy increases, starting from almost 50% of probability at 2 eV and reaching 90% at 4.5 eV. Conversely, the likelihood that either of the exchange reactions would occur decreases monotonically with collision energy: in that same range,  $\Pi_1$  ( $H_a/H_b$  exchange) goes from 40% to 4.5% and  $\Pi_2$  ( $H_a/D$  exchange) falls from 5% to 0.5%.

The overall reaction probabilities are evaluated by taking the integrals of  $\phi_1$ ,  $\phi_2$  and  $\phi_3$  over all the energies (the integral of  $\Delta$  is one). In total, if the experiment were to be repeated infinitely many times, the non-reactive scattering would occur 76.5% of the time against only 21.2% and 2.3% of exchange reactions releasing a protium or a deuterium, respectively, which is consistent with the values obtained from the time-resolved fluxes. The discrepancy between the two sets of values is probably due to the fact that the flux  $\phi_3$  is overestimated at the tails of the energy distribution, making the sum of the three fluxes larger than the latter (which is why we performed additional propagations at lower and higher collision energies for the calculation of energy-resolved probabilities). The overestimation seemed to be larger with a longer CAP in the non-reactive scattering channel ‘3’.

As  $H_a$  approaches  $H_bOD$ , the regions of the  $H_3O$  PES explored by the wavepacket are characterized by the presence of a barrier whose geometry at the saddle point is of  $C_s$  symmetry. The latter is followed by a shallow local minimum with a geometry of  $C_{3v}$  symmetry. The energies of these two are, respectively, 0.888 eV and 0.789 eV above the  $H + H_2O$  asymptote.<sup>100</sup> From that  $C_{3v}$  intermediate, the paths leading to the departure of either hydrogen atom originally bound to the oxygen are the same as the one just described, backwards. Now, even though the collision en-

ergy here is well beyond the barrier, it appears that the exchange would fail most of the time and non-reactive scattering would occur, in particular for the high energy components of the wavefunction. The collision is so intense that the kinetic energy stored in the  $R_3$  degree of freedom – as  $H_a$  is quickly approaching  $H_bOD$  – seems not to have sufficient time to redistribute within the  $H_2DO$  transient. Little energy is passed to the O– $H_b$  and O–D bonds. The collision is dominated by the repulsion between  $H_a$  and O and is characterized by the very short rise-time in the probability of non-reactive scattering.

Nevertheless, a small fraction of the wavefunction succeeds in following either exchange process as in eq. (1). Protium-to-protium exchange is clearly preferred to protium-to-deuterium. Yet, the direction of attack of  $H_a$  towards  $H_bOD$  is along the  $C_2$  axis of the latter, so  $H_b$  and D are geometrically equivalent prior to the collision.  $H_b$  and D being isotopes, for any position of  $H_a$  in that axis the potential energy on either bond dissociation channel is the same.

A possible explanation of the difference in exchange reaction probabilities could be a manifestation of vibrational zero-point energy effects within the  $H_aH_bOD$  transient. Indeed, the normal modes of the HOD molecule alone are localized, featuring distinct O–H and O–D stretching modes with well-separated vibrational frequencies (3707.47  $\text{cm}^{-1}$  and 2723.68  $\text{cm}^{-1}$ , respectively<sup>105</sup>). Their contributions to the overall vibrational zero-point energy are therefore substantially different. By the harmonic approximation, their difference can be estimated at 491.895  $\text{cm}^{-1}$ , i.e. 0.0609872 eV. This suggests that more energy is required to dissociate the O–D bond than the O–H one. This analogy can be applied to the  $[H_aH_bOD]^\ddagger$  saddle point structures on the PES. The geometries at the saddle points of  $H_3O$  with  $C_s$  symmetry are very similar to the one at the  $C_{3v}$  local minimum, the main difference being that one of the hydrogen atoms (the one in the symmetry plane) is a bit farther than the other two from the oxygen. The imaginary frequency normal mode is essentially the stretching of the bond in that plane. The vibrational zero-point energy at that saddle point stems from contributions of the other normal modes. Now, the electronic barriers from the  $H_aH_bOD$  local minimum to the  $[(H_aOD)H_b]^\ddagger$  and  $[(H_aOH_b)D]^\ddagger$  saddle points are the same, but the vibrational zero-point energies are different, resulting in an effective barrier height difference. This is supported by inspection of harmonic frequencies calculated at the MP2/aug-cc-pvtz level of theory with the Gaussian16 quantum chemistry package,<sup>106</sup> where this difference is estimated at 492.62  $\text{cm}^{-1}$ , that is 0.0611 eV.

However, this difference is much smaller than the collision energies at play in the present case. As a result, if it had a role in the selectivity between the two exchange outcomes, one would expect the ratio  $\Pi_1/\Pi_2$  to be close or at least approach unity from above for higher and higher collision energies. This is not the observed trend (that ratio is significantly larger than 1 and increases with the collision energy).

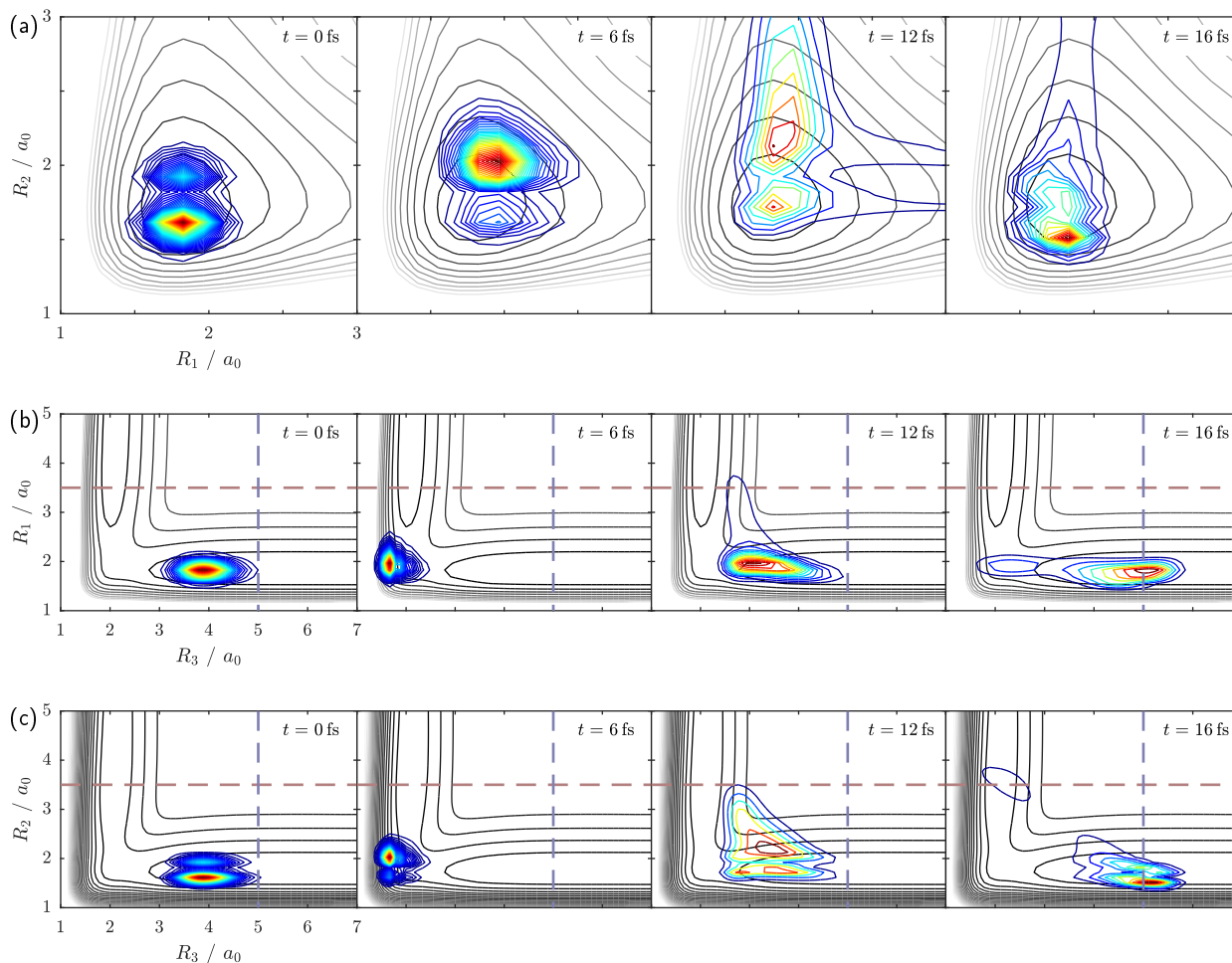


Fig. 8 Same as fig. 3, with initial OD-stretching mode excitation of HOD.

## 6.2 Propagation from vibrationally pre-excited HOD

In section 6.1 we mentioned that vibrational zero-point energy effects may play a role in the selectivity between either reaction channels (among what is left aside non-reactive scattering). In order not to entirely reject this possibility, we ran an additional propagation in the same conditions as described in section 6.1, except that the initial state was excited to the first OD-stretching mode vibrational state of HOD. The excitation is applied to the relaxed ground state geometry wavefunction  $\psi_g$  by using a harmonic oscillator raising ladder operator (the excitation energy is  $2824.5 \text{ cm}^{-1}$  in the harmonic approximation<sup>107</sup>) along the  $R_2$  coordinate (which is approximately the same as the actual OD-stretching normal mode coordinate). The time evolution of the marginal probability densities for this propagation are shown in fig. 8. Initially, the wavepacket is located in the same region as before, in the entrance channel, but it now features a node and a larger spread along the  $R_2$  coordinate as a result of the vibrational excitation. The collision occurs in the same way as in the previous case with the exception that there is now a much larger fraction of the wavepacket that goes into the O–D bond dissociation reaction channel (see fig. 8a at  $t = 12 \text{ fs}$  and compare the tails of the marginal probability densities in fig. 8b and fig. 8c). Non-reactive scattering is still predominant and the O–H bond dissociation is

again observable, yet in minor proportion compared to the O–D bond dissociation.

By the look of the time-resolved fluxes and reaction probabilities (fig. 9) it is clear that non-reactive scattering is still the main observed outcome, with a steep rise of  $P_3$ , the time-integrated flux in the non-reactive scattering channel, from nearly zero to 90% of its asymptotic value (63.2%) within the timespan between 8 fs to 16 fs. The selectivity between  $\text{H}_a/\text{H}_b$  and  $\text{H}_a/\text{D}$  exchange reactions is reversed. The flux  $F_1$  in the O– $\text{H}_b$  bond dissociation channel peaks at the same time as the one along the non-reactive scattering channel. The flux  $F_2$  along the O–D bond dissociation channel increases again 3 to 4 fs later but is now more prominent than in the previous propagation. The integrals  $P_1$  and  $P_2$  of the fluxes  $F_1$  and  $F_2$  increase with the same time constants as in the previous propagation. The final values are respectively 12.0% and 24.8%.

The energy-resolved data is shown in fig. 10. The tails of the reaction probabilities in fig. 10a are obtained by the same technique as explained in the previous section, by setting  $p'_{\text{exc}}$  to 17.5 a.u. and 20.5 a.u., and choosing the junction points to be  $(\epsilon_{\ominus}, \epsilon_{\oplus}) = (2.7, 3.9) \text{ eV}$ . The collision energy distribution  $\Delta$  is essentially unchanged from the previous propagation and the fluxes preserve the same bell-shaped feature, though the magnitude of

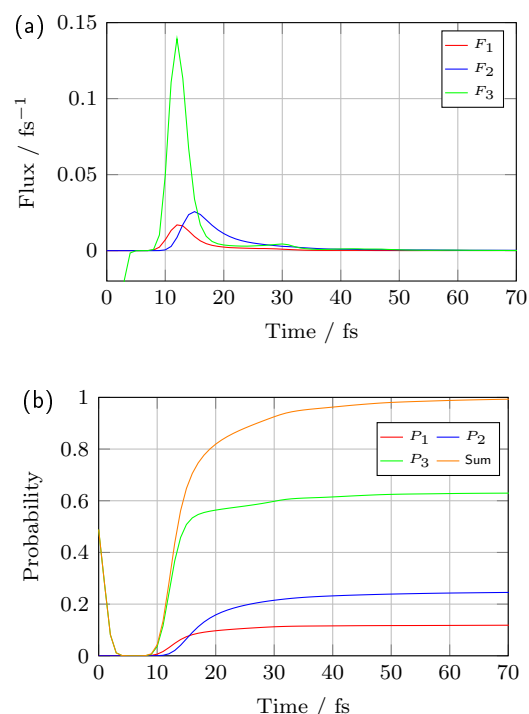


Fig. 9 Time-resolved (a) fluxes and (b) reaction probabilities as in fig. 6, with initial OD-stretching mode excitation of HOD.

$\phi_2$  is now larger than  $\phi_1$  over the whole relevant energy range (see fig. 10a). The resulting reaction probabilities (fig. 10b) show the same energy dependence, i.e. the probability of non-reactive scattering  $\Pi_3$  increases with energy (from 44% to 87.5% in the shown range) and the probabilities of both exchange reaction success  $\Pi_1$  or  $\Pi_2$  decrease monotonically (from 21% to 6.5% for the former and from 35% to 9% for the latter). A noteworthy difference with the situation with the vibrational ground state of HOD, apart from the fact that now  $\Pi_1$  and  $\Pi_2$  are reversed, is that the ratio  $\Pi_1/\Pi_2$  does tend to one (from below). The overall energy-integrated reaction probabilities are 69% for the non-reactive scattering, 11.5% for the  $H_a/H_b$  exchange and 19.5% for the  $H_a/D$  exchange, again fairly close to the values calculated in the time-dependent picture, given the uncertainty explained earlier.

By exciting the OD-stretching mode, the vibrational energy of HOD, thus that of the  $H_aH_bOD$  transient, are increased by one quantum carried by the OD bond. As a result, the effective barrier height at the  $[(H_aOD)H_b]^\ddagger$  saddle point is increased and is now larger than at the other  $[(H_aOH_b)D]^\ddagger$  point. This fact eventually makes the O– $H_b$  bond harder to break. Moreover, this propagation matches better the expectation that the vibrational energy within the  $H_aH_bOD$  transient plays less and less a role as the collision energy increases, since the difference in effective barrier height becomes negligible. One last point about this propagation is that it is an interesting illustration of how one could control the selectivity of the reaction by changing the quantum state of its colliding moieties, also known as mode-selective chemistry.<sup>40–42</sup>

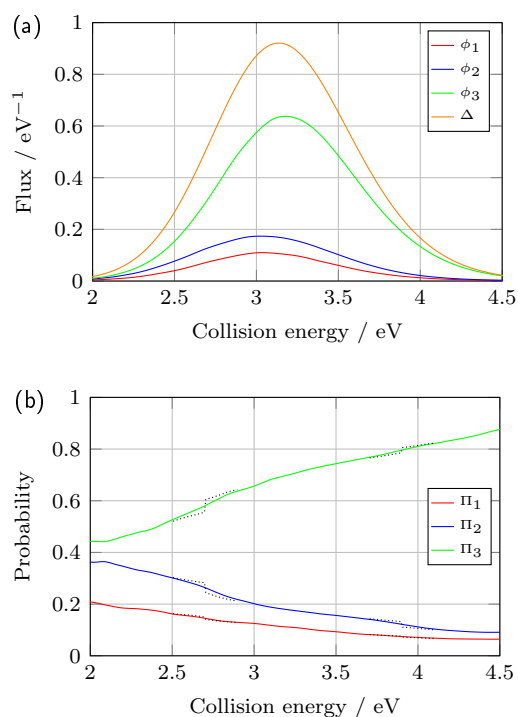


Fig. 10 Energy-resolved (a) fluxes and wavepacket energy distribution  $\Delta$  and (b) reaction probabilities, with initial OD-stretching mode excitation of HOD. The dotted lines represent the original data around the junction points which has been smoothed with switching functions.

### 6.3 Propagation at lower collision energy

In order to connect our study to pre-existing work on these exchange reactions,<sup>32</sup> another propagation, this time at lower collision energy, was carried out. The value of  $p'_{exc}$  was lowered to 11 atomic units so that the collision energy distribution of the wavepacket would cover a range centered at the exchange reaction barrier height. The time-resolved fluxes and reaction probabilities are shown in fig. 11. The time-scale of the reaction is visibly longer, as there is still 5% of chances of finding the system inside the interaction region at  $t = 100$  fs (see fig. 11b). The non-reactive scattering probability  $P_3$  evolves in two steps: a neat increase between 15 and 22 fs and another slower one at later times. These correspond respectively to the first peak in flux  $F_3$  at 19 fs and the following slow undulating decrease which matches with the flux  $F_1$  on the O– $H_b$  bond dissociation channel (see fig. 11a). This suggests that the first fast phase corresponds to the portion of the wavepacket that is immediately reflected by the potential barrier and that the second one is due to the other portion which is retained in the interaction region and eventually splits into two parts which mainly go either towards the non-reactive scattering channel or the O– $H_b$  bond dissociation channel. This splitting is confirmed by inspection of the wavepacket (not shown). Furthermore, we do not observe abstraction reactions. The energy-resolved fluxes are richer in features than in the propagations carried out above (fig. 12a). The reaction probabilities shown in fig. 12b support the previous argument, as most of the components of the wavepacket with energies below the barrier height are reflected with certainty and, for the ones above it, there is

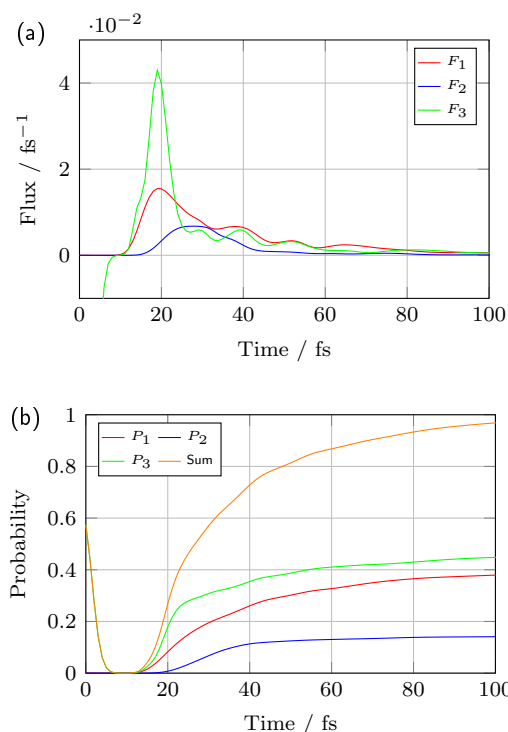


Fig. 11 Time-resolved (a) fluxes and (b) reaction probabilities for the exchange reaction at low collision energy.

a competition mostly between non-reactive scattering and O–H<sub>b</sub> bond dissociation. The shift in the onset of  $\Pi_2$  relative to that of  $\Pi_1$  is consistent with the higher barrier for O–D dissociation.

The positions of the features at 0.92, 0.96 and 1.0 eV in fig. 12b are close to the ones found by Fu and Zhang<sup>32</sup> on a similar PES<sup>108</sup> and are ascribed to shape resonances<sup>109</sup> due to the shape of the potential around the  $C_{3v}$  local minimum after the barrier. The differences in the magnitudes between our propagation and their study is due to the fact that their results are obtained by averaging over different orientations, whereas our study involves a well-defined initial wavefunction describing a specific geometrical arrangement of the atoms. The latter is favourable for a backside attack of the H<sub>a</sub> against the oxygen, which explains why both H<sub>a</sub>/H<sub>b</sub> and H<sub>a</sub>/D exchange reaction probabilities obtained here are overall twice as large as in their full-collision study. The ratio between reaction probabilities of either exchange processes (channels ‘1’ vs. ‘2’) is consistent with their results.

#### 6.4 The effect of multiple collisions

As in section 6.1 we could not exclude completely that more than one collision between H<sub>a</sub> against H<sub>b</sub>OD would occur, we looked at the opposite limit situation (case (ii) mentioned in section 6.1): the H<sub>a</sub> atom remains in the Cl–O axis after the first collision and is thus pushed back again by the Cl atom towards H<sub>b</sub>OD. This model is simply implemented by replacing the CAP ‘3’ by a 1-D repulsive potential, depending on  $R_3$  only, which forces the wavepacket to return towards the reaction region. Here, this repulsive potential is an adapted form of that of H<sub>a</sub>Cl in the  $A^1\Pi$  state (see appendix C). The same initial conditions as in section 4

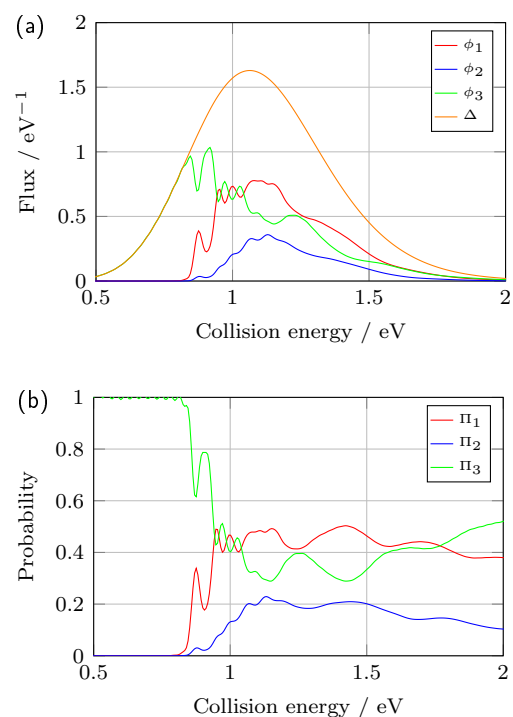


Fig. 12 Energy-resolved (a) fluxes and wavepacket energy distribution  $\Delta$  and (b) reaction probabilities for the low collision energy propagation.

were kept and this repulsive potential was activated at  $t = 6$  fs, as was done for CAP ‘3’ in section 6.1. The resulting time-evolution of the reduced densities as functions of  $R_1$ ,  $R_2$  and  $R_3$  is shown in fig. 13.

By construction, the propagation up to  $t = 6$  fs is identical to that discussed in section 6.1. Shortly after, the wavepacket follows the same path as in section 6.1, i.e. it mainly enters channel ‘3’, corresponding to non-reactive scattering, although a small fraction enters channel ‘1’, corresponding to H<sub>a</sub>/H<sub>b</sub> exchange. However, here, the wavepacket moves back to the reaction region (see figs. 13b and 13c at  $t = 20$  fs) and a second H<sub>a</sub> + H<sub>b</sub>OD collision occurs around  $t = 24$  fs. From this, a significant portion goes to channel ‘2’, corresponding to H<sub>a</sub>/D exchange (see figs. 13a and 13c at  $t > 28$  fs), while only little H<sub>a</sub>/H<sub>b</sub> exchange can be noticed. The remaining part of the wavepacket keeps oscillating along the  $R_3$  coordinate in and out of the reaction region. The behaviour with respect to the angular coordinates  $\beta_s$  and  $\gamma_s$  (not shown) is similar to that displayed in figs. 4 and 5 up to  $t = 16$  fs and the reduced densities hardly change at later times.

The time-resolved fluxes and their integrated forms, shown in fig. 14, confirm these observations. Right after the first collision occurring at 6 fs, the fluxes across the boundaries of the reaction region behave like those in fig. 6, i.e. a strong increase of the flux  $F_3$  (corresponding to non-reactive scattering), a weaker increase of  $F_1$  (H<sub>a</sub>/H<sub>b</sub> exchange) reaching a local maximum at 13 fs and a barely noticeable increase of  $F_2$  (H<sub>a</sub>/D exchange). However, since now CAP ‘3’ is replaced by the repulsive confining potential, the wavepacket comes back inside the reaction region, the flux  $F_3$  across its boundary at  $R_3 = d$  changes sign and its integrated form  $P_3$  goes back to zero (up to an integration error of 0.02). Next,  $F_1$

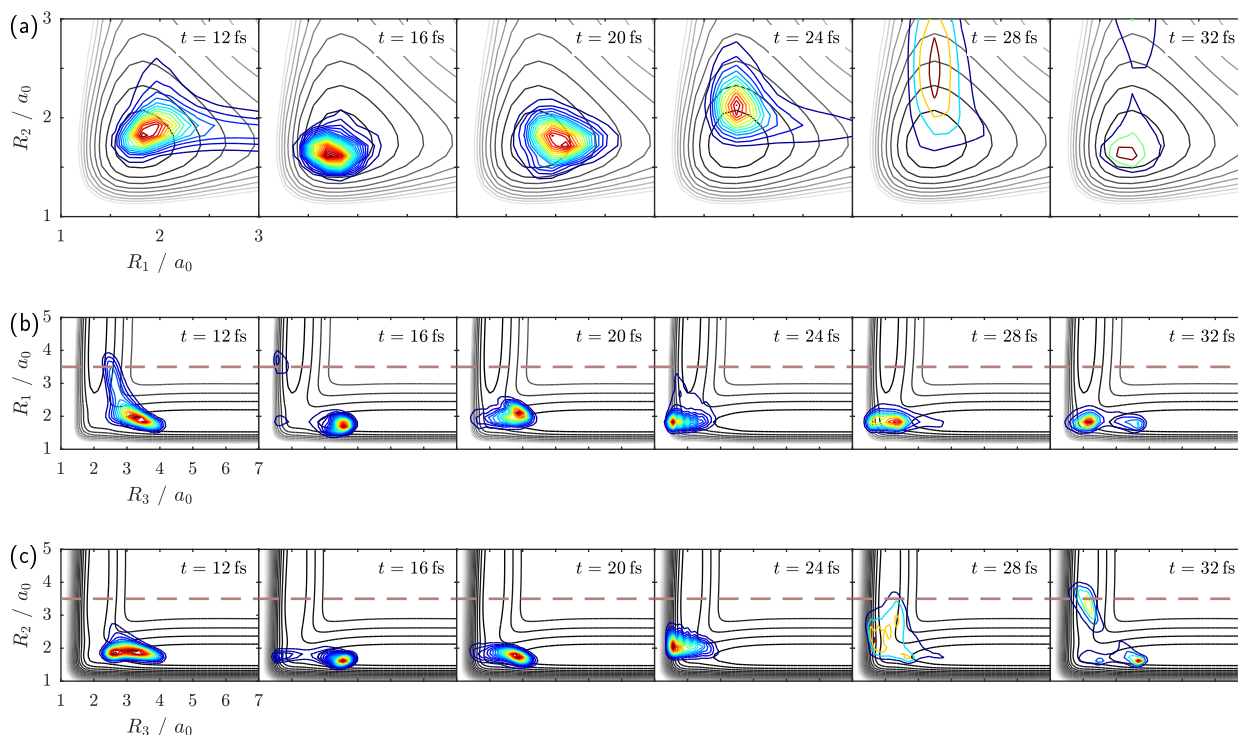


Fig. 13 Same as fig. 3, but CAP '3' is replaced by a repulsive potential at the end of the grid in  $R_3$  (not represented, see appendix C for details). The densities at  $t = 0$  and  $t = 6$  fs are identical to those shown in fig. 3. The dashed lines indicates the beginning of either CAP '1' or CAP '2'.

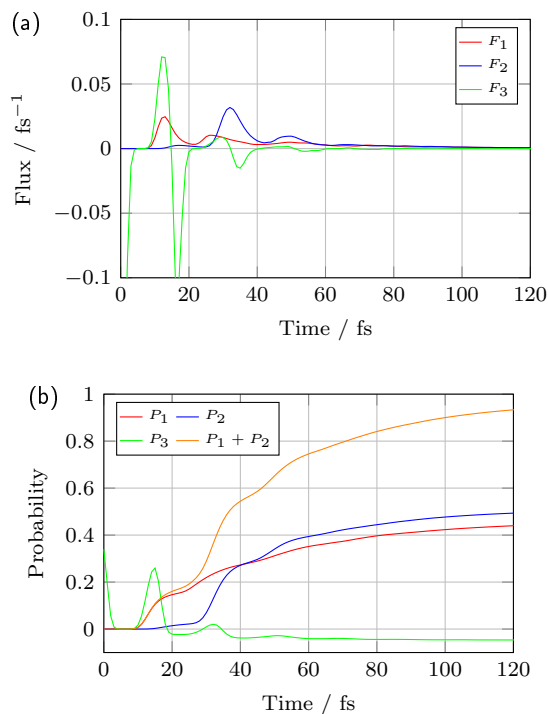


Fig. 14 Time-resolved (a) fluxes and (b) reaction probabilities as in fig. 6, but CAP '3' is replaced by a repulsive potential at the end of the grid in  $R_3$  (see appendix C for details).

reaches another local maximum at 26 fs and  $F_2$  does too at 32 fs, while  $F_3$  features another oscillation. The time-integrated quantities  $P_1$ ,  $P_2$  and  $P_3$  show that it is now the  $H_a/D$  exchange process which is predominant. More importantly, because of this second collision, the overall selectivity between  $H_a/H_b$  and  $H_a/D$  exchanges is lost. As further collisions unfold for the remainder of wavepacket, the latter reaction ends up to be slightly more probable than the former. A measure of the time-scale of the whole process in this particular case can be given by the timespan over which  $P_1 + P_2$  increases up to 90% of its asymptotic value, which is 84 fs (between  $t = 10$  fs and  $t = 94$  fs). Note though that the increase occurs in successive steps rather than following a smooth exponentially convergent curve. This time-scale is much longer, by one order of magnitude, than in the previous propagation (section 6.1) i.e. without the confining repulsive potential cast by Cl. This elongation is the result of repeated collisions between  $H_a$  and  $H_bOD$  forced by the presence of this potential, eventually leading a larger fraction of the wavepacket to enter either exchange reaction channel.

Hence, if Cl had to play a role in the dynamics of the collision between  $H_a$  and  $H_bOD$ , by confining the former in the vicinity of the latter, two main effects would be noticeable: (a) loss of selectivity between  $H_a/H_b$  and  $H_a/D$  exchange reactions and (b) step-wise increase of the exchange reaction probabilities with a resulting stretching of the overall reaction time-scale.

## 7 Conclusion

Femtochemistry experiments of bimolecular reactions initiated by intramolecular photolysis of weakly bound complexes are now

between twenty and thirty years old and have not further been studied in detail. In this attempt of reviving the interest in these, we studied the selectivity of the exchange reactions  $\text{H} + \text{H}'\text{OD} \longrightarrow \text{HOD} + \text{H}'/\text{H}'\text{OH} + \text{D}$  initiated by performing the  $(\text{HCl}) \cdots (\text{HOD})$  hydrogen-bound complex and photodissociating the HCl moiety.

The photodissociation of HCl causes a release of a considerable amount of energy in the form of translational collision energy between its hydrogen atom and the HOD partner. Because of the magnitude of that energy, the repulsion between the approaching hydrogen and the oxygen belonging to the latter dominates in this collisional process, mainly leading to non-reactive scattering. It is shown that, after the collision, the hydrogen atom of HCl does most likely not encounter the Cl atom again, indicating that additional multiple collisions between H and H'OD are not expected. However, H-to-H' and H-to-D exchange processes can still be observed, with a distinguishable preference of the former to the latter. This selectivity can be controlled by changing the vibrational state of HOD. We tentatively ascribe the selectivity to vibrational effects in virtue of the fact that O–H and O–D vibrations contribute in different amounts to the vibrational zero-point energy of the  $\text{H}_2\text{DO}$  transient. The time-scales of the non-reactive scattering and exchange processes are very short: less than 6 fs for non-reactive scattering and H-to-H' exchange and less than 27 fs for H-to-D exchange. Our results were also compared to previous full-collision studies of the title reaction at lower collision energies. We find, in particular, that the probability for the exchange reactions to occur is enhanced.

Due to the assumption of a fully dissociated HCl prior to the bimolecular collision, the time-scales given above are lower-limit estimates. Indeed, by forcing the incoming H atom to collide multiple times against H'OD, with the addition of the repulsive potential stemming from the presence of the stationary Cl atom (see section 6.4 and appendix C), the overall probability of occurrence of either exchange reaction increases. The resulting overall time-scale of the process is then one order of magnitude longer than if it is limited to only one collision. Moreover, if multiple collisions occur, the selectivity between H-to-H' and H-to-D exchanges becomes less pronounced. Although the additional collisions are not expected to occur in this specific system, further studies which explicitly include the chlorine atom and make use of the full excited state PES are needed to clarify this aspect. On the other hand, the interesting results shown in section 6.4 suggest that these multiple collisions may strongly impact the outcome of precursor-initiated reactions in other similar weakly bound systems.

## Conflicts of interest

There are no conflicts to declare.

## Acknowledgments

The authors are grateful to Hans-Dieter Meyer, Markus Schröder and Steve Ndengué for their support in using MCTDH, Joel Bowman and Qi Yu for providing the potential energy surface of  $(\text{HCl}) \cdots (\text{H}_2\text{O})$  and help in its usage, Johan Schmidt and Gunnar Nyman for providing the potential energy curves of HCl, Jun Chen for providing the potential energy surface

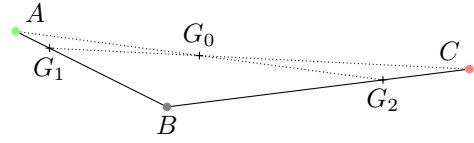


Fig. 15 Simplified representation of the generic  $A-B \cdots C$  complex and the associated centers of masses:  $G_0$  is the center of mass of  $\{A, B, C\}$ ,  $G_1$  is the center of mass of  $\{A, B\}$  and  $G_2$  is the center of mass of  $\{B, C\}$ . In this work,  $A = \text{Cl}$ ,  $B = \text{H}_a$  and  $C = \text{G}_s$  (see fig. 1). Here, the positions of the points  $A$ ,  $B$  and  $C$ , as well as their weights, are arbitrarily chosen for visualization purposes.

of  $\text{H}_3\text{O}$  and help in its usage and the DTU Computing Center for access to the High Performance Computing services. The rendering of  $(\text{HCl}) \cdots (\text{HOD})$  in fig. 1 was made with Speck (<http://www.tyro.github.io/speck/>).

## A Calculation of the initial momentum $\mathbf{p}'_{\text{exc}}$

In this appendix we refer to fig. 15. For convenience, we replace the atoms Cl and  $\text{H}_a$  by two points  $A$  and  $B$  as well as the center of mass of  $\text{H}_b\text{OD}$  by a point  $C$ . These points carry masses  $m_A = m_{\text{Cl}}$ ,  $m_B = m_{\text{H}_a}$  and  $m_C = m_{\text{H}_b\text{OD}}$ , respectively. We call  $G_0$ ,  $G_1$  and  $G_2$  the centers of masses of the groups of points  $\{A, B, C\}$ ,  $\{A, B\}$  and  $\{B, C\}$ , respectively, and define the space-fixed frames of reference  $\mathcal{F}_0$ ,  $\mathcal{F}_1$  and  $\mathcal{F}_2$  centered at these points. We recall the definitions of the points: for any arbitrary point  $X$  in space, we have

$$\overrightarrow{G_0 X} = \frac{m_A \overrightarrow{AX} + m_B \overrightarrow{BX} + m_C \overrightarrow{CX}}{m_A + m_B + m_C} \quad (32)$$

$$\overrightarrow{G_1 X} = \frac{m_A \overrightarrow{AX} + m_B \overrightarrow{BX}}{m_A + m_B} \quad (33)$$

$$\overrightarrow{G_2 X} = \frac{m_B \overrightarrow{BX} + m_C \overrightarrow{CX}}{m_B + m_C} \quad (34)$$

We denote by  $\vec{p}_X^{(n)}$  the classical momentum of the point  $X$  in the frame  $\mathcal{F}_n$ , that is:

$$\vec{p}_X^{(n)} = m_X \frac{d\overrightarrow{G_n X}}{dt} \quad (35)$$

We assume, on the one hand, that the whole system is initially at rest in  $\mathcal{F}_0$  (and therefore also in  $\mathcal{F}_1$  and  $\mathcal{F}_2$ ) and, on the other hand, that the interaction between  $\text{H}_a\text{Cl}$  and  $\text{H}_b\text{OD}$  (hence between  $\{A, B\}$  and  $C$ ) does not play a role in the dissociation and the dynamics (except for their placement with respect to each other). Thus, the subsequent dissociation of  $\{A, B\}$  at total zero momentum in  $\mathcal{F}_1$  implies  $\vec{p}_A^{(1)} = -\vec{p}_B^{(1)}$ . Moreover, the conversion of the excess potential energy  $\Delta V_{\text{exc}}$  (see section 2) in kinetic energy yields:

$$\Delta V_{\text{exc}} = \frac{(\vec{p}_A^{(1)})^2}{2m_A} + \frac{(\vec{p}_B^{(1)})^2}{2m_B} = \frac{(\vec{p}_B^{(1)})^2}{2} \left( \frac{1}{m_A} + \frac{1}{m_B} \right) \quad (36)$$

As a consequence:

$$p_{\text{exc}} := \left\| \vec{p}_B^{(1)} \right\| = \sqrt{2\mu_{AB}\Delta V_{\text{exc}}} \quad (37)$$

with  $\mu_{AB}^{-1} = m_A^{-1} + m_B^{-1}$ . Again, since we assume that  $\{A, B\}$  and  $C$  do not interact, the momenta of  $G_1$  and  $C$  are zero in  $\mathcal{F}_0$ , that is:

$$\vec{p}_{G_1}^{(0)} = \vec{p}_C^{(0)} = \vec{0} \quad \text{i.e.} \quad \frac{d\vec{G}_0\vec{G}_1}{dt} = \frac{d\vec{G}_0\vec{C}}{dt} = \vec{0} \quad (38)$$

We are now in the position of calculating the translational collision energy between  $B$  and  $C$  in the frame of reference  $\mathcal{F}_2$ . The latter is given by:

$$E_{\text{coll}} = \frac{(\vec{p}_B^{(2)})^2}{2m_B} + \frac{(\vec{p}_C^{(2)})^2}{2m_C} = \frac{1}{2}m_B \left( \frac{d\vec{G}_2\vec{B}}{dt} \right)^2 + \frac{1}{2}m_C \left( \frac{d\vec{G}_2\vec{C}}{dt} \right)^2 \quad (39)$$

The two derivatives can be expressed in terms of  $\vec{p}_B^{(1)}$  by using eqs. (34), (35) and (38):

$$\begin{aligned} \frac{d\vec{G}_2\vec{B}}{dt} &= \frac{d}{dt} (\vec{G}_2\vec{G}_1 + \vec{G}_1\vec{B}) \\ &= \frac{d}{dt} \left( \frac{1}{m_B + m_C} (m_B\vec{B}\vec{G}_1 + m_C\vec{C}\vec{G}_1) \right) + \frac{\vec{p}_B^{(1)}}{m_B} \\ &= \frac{m_B}{m_B + m_C} \frac{d\vec{B}\vec{G}_1}{dt} + \frac{m_C}{m_B + m_C} \frac{d\vec{C}\vec{G}_1}{dt} + \frac{\vec{p}_B^{(1)}}{m_B} \\ &= -\frac{\vec{p}_B^{(1)}}{m_B + m_C} + \frac{m_C}{m_B + m_C} \frac{d}{dt} (\underbrace{\vec{C}\vec{G}_0 + \vec{G}_0\vec{G}_1}_{=\vec{0}}) + \frac{\vec{p}_B^{(1)}}{m_B} \\ &= \vec{p}_B^{(1)} \left( \frac{1}{m_B} - \frac{1}{m_B + m_C} \right) \end{aligned}$$

and

$$\begin{aligned} \frac{d\vec{G}_2\vec{C}}{dt} &= \frac{d}{dt} (\vec{G}_2\vec{G}_1 + \vec{G}_1\vec{C}) \\ &= \frac{d}{dt} \left( \frac{1}{m_B + m_C} (m_B\vec{B}\vec{G}_1 + m_C\vec{C}\vec{G}_1) \right) + \frac{d}{dt} (\underbrace{\vec{G}_1\vec{G}_0 + \vec{G}_0\vec{C}}_{=\vec{0}}) \\ &= -\frac{\vec{p}_B^{(1)}}{m_B + m_C} + \frac{m_C}{m_B + m_C} \frac{d}{dt} (\underbrace{\vec{C}\vec{G}_0 + \vec{G}_0\vec{G}_1}_{=\vec{0}}) = -\frac{\vec{p}_B^{(1)}}{m_B + m_C} \end{aligned}$$

Plugging these relations back into eq. (39) and by using eq. (37):

$$\begin{aligned} E_{\text{coll}} &= \frac{1}{2}m_B \left( \vec{p}_B^{(1)} \left( \frac{1}{m_B} - \frac{1}{m_B + m_C} \right) \right)^2 + \frac{1}{2}m_C \left( -\frac{\vec{p}_B^{(1)}}{m_B + m_C} \right)^2 \\ &= \frac{\|\vec{p}_B^{(1)}\|^2}{2} \left( m_B \left( \frac{1}{m_B} - \frac{1}{m_B + m_C} \right)^2 + m_C \left( \frac{1}{m_B + m_C} \right)^2 \right) \\ &= \frac{p_{\text{exc}}^2}{2} \left( m_B \left( \frac{m_C}{m_B(m_B + m_C)} \right)^2 + m_C \left( \frac{1}{m_B + m_C} \right)^2 \right) \end{aligned}$$

$$\begin{aligned} &= \Delta V_{\text{exc}} \cdot \mu_{AB} \cdot \left( \frac{m_C}{m_B + m_C} \right)^2 \cdot \left( \frac{1}{m_B} + \frac{1}{m_C} \right) \\ &= \Delta V_{\text{exc}} \cdot \frac{m_A m_B}{m_A + m_B} \cdot \frac{m_C^2}{(m_B + m_C)^2} \cdot \frac{m_B + m_C}{m_B m_C} \end{aligned}$$

that is

$$E_{\text{coll}} = \Delta V_{\text{exc}} \cdot \frac{m_A}{m_A + m_B} \cdot \frac{m_C}{m_B + m_C} \quad (40)$$

Finally, we need to determine the initial conjugated momentum  $\vec{p}_3$  associated to the orthogonal vector  $\vec{R}_3$ . Since we have simply  $\vec{R}_3 = \vec{C}\vec{B}$ , then by eqs. (32) and (33):

$$\vec{R}_3 = \frac{1}{m_C} \left( (m_A + m_B + m_C)\vec{G}_0\vec{B} - (m_A + m_B)\vec{G}_1\vec{B} \right) \quad (41)$$

Therefore,

$$\begin{aligned} \vec{p}_3 &= \mu_3 \frac{d\vec{R}_3}{dt} \\ &= \mu_3 \cdot \frac{1}{m_C} \left( (m_A + m_B + m_C) \frac{d\vec{G}_0\vec{B}}{dt} - (m_A + m_B) \frac{d\vec{G}_1\vec{B}}{dt} \right) \\ &= \frac{\mu_3}{m_C} \left( (m_A + m_B + m_C) \left( \underbrace{\frac{d\vec{G}_0\vec{G}_1}{dt}}_{=\vec{0}} + \frac{d\vec{G}_1\vec{B}}{dt} \right) - (m_A + m_B) \frac{d\vec{G}_1\vec{B}}{dt} \right) \\ &= \frac{m_B m_C}{m_B + m_C} \cdot \frac{d\vec{G}_1\vec{B}}{dt} = \frac{m_C}{m_B + m_C} \cdot \vec{p}_B^{(1)} \end{aligned}$$

and finally we obtain:

$$p'_{\text{exc}} := \|\vec{p}_3\| = \frac{m_C}{m_B + m_C} \cdot p_{\text{exc}} \quad (42)$$

## B Correctness of the kinetic energy operator and calculation of the zero-point energy of HOD

Before proceeding to any of the simulations that are presented in this article, we made sure that the (not self-evident) kinetic energy operator  $\hat{T}_{\text{HOD}}$  in eq. (12) and its implementation in the MCTDH package was correct by preliminary numerical tests on HOD. To that end, we modified the PES of the system  $\text{H}_3\text{O}$  by Chen *et al.*<sup>100</sup> by fixing the  $R_3$ ,  $\beta_s$  and  $\gamma_s$  coordinates such that  $\text{H}_a$  would be far from HOD. The resulting effective surface is, in fact, the one of regular water expressed as a function of  $R_1$ ,  $R_2$  and  $u$ . This surface was adapted in the MCTDH format with POTFIT on a grid with the same specifications as in table 1 for these coordinates, without mode combinations and by including all possible natural potentials. The Hamiltonian of HOD was then taken as the sum of this potential and the kinetic energy operator  $\hat{T}_{\text{HOD}}$ . A block relaxation was carried out in order to calculate the first 11 rotational excited states of HOD. The rotational lines listed in the MARVEL database<sup>110–112</sup>, taken as an experimental reference, could unequivocally be assigned to energy differences between the calculated eigenstates.

The vibrational zero-point energy of HOD could be calculated by an improved relaxation on that same modified surface and by keeping only the terms of  $\hat{T}_{\text{HOD}}$  depending on  $R_1$ ,  $R_2$  and  $u$  (thus

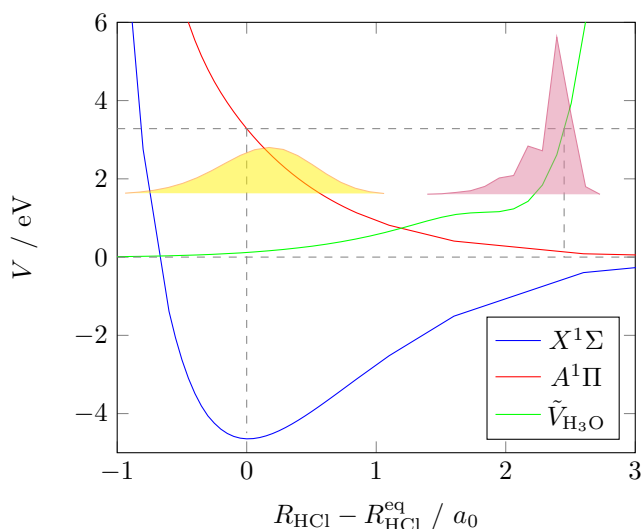


Fig. 16 Ground (blue) and excited (red) states potentials of HCl,<sup>77</sup> cut of the potential of H<sub>3</sub>O (green) and the reduced density of the wavepacket along  $R_3$  at  $t = 0$  fs (yellow) and  $t = 6$  fs (purple) in the main propagation. The zero in abscissa is the Franck-Condon point of H<sub>a</sub>Cl. The cut of the H<sub>3</sub>O potential, originally a function of the radial distance  $R_3$  at fixed values of the other coordinates (expectation values at  $t = 0$  fs), has been flipped and shifted horizontally by the expectation value of  $R_3$  at  $t = 0$  fs. The zero in the ordinate corresponds to the asymptotic values of the potentials at  $R_{\text{HCl}} \rightarrow \infty$  and infinitely separated H + H<sub>2</sub>O. Dashed lines mark the Franck-Condon point and the “turning point”.

forcing the molecule to be in its rotational ground state). The obtained value is 0.498389 eV.

### C Acceleration of H<sub>a</sub> during the photodissociation of H<sub>a</sub>Cl

In the initial state of the main propagation (eq. (14)), the acceleration of the H<sub>a</sub> atom via the photodissociation of H<sub>a</sub>Cl is represented by the factor  $\exp(-ip'_{\text{exc}}R_3/\hbar)$ , with  $p'_{\text{exc}}$  being the (classical) linear momentum of H<sub>a</sub> in the space-fixed frame of reference of H<sub>a</sub>H<sub>b</sub>OD calculated as in appendix A. The computed value is given by considering that H<sub>a</sub>Cl has fully dissociated before H<sub>a</sub> encounters H<sub>b</sub>OD. In other words, the used value is an upper bound of the “true” one. However, this does not affect significantly the outcome of the propagations described in this work.

Assuming that Cl, H<sub>a</sub>, and O are aligned, that  $R_3 \approx R_{\text{OH}_a}$  and that  $R_{\text{H}_a\text{Cl}} + R_{\text{OH}_a} = \text{constant}$ , fig. 16 illustrates how far the H<sub>a</sub> atom goes in the H<sub>a</sub>Cl dissociation curve while approaching H<sub>b</sub>OD. The wavepacket indeed reaches the H<sub>a</sub>H<sub>b</sub>OD transition state barrier before H<sub>a</sub>Cl has fully dissociated. However, because of the large initial potential energy at the Franck-Condon geometry, the wavepacket easily overcomes the barrier and reaches the turning point on the H<sub>a</sub>H<sub>b</sub>OD potential which corresponds to almost full dissociation of H<sub>a</sub>Cl. Hence, by the definition of the initial state as in eq. (14), we are introducing only marginal errors concerning the accessible regions on the H<sub>a</sub>H<sub>b</sub>OD PES. The energy-resolved reaction probabilities are thus not expected to be much different from those shown in fig. 7.

In eq. (14) we are omitting the actual acceleration of H<sub>a</sub> from

the Franck-Condon geometry of H<sub>a</sub>Cl, that is, the increase of momentum of H<sub>a</sub> over time. Nevertheless, we expect that only the initial delay time before H<sub>a</sub> and H<sub>b</sub>OD collide will be impacted, namely, it will take longer for H<sub>a</sub> to reach H<sub>b</sub>OD than shown in fig. 6.

Note that the repulsive potential used in the propagation discussed in section 6.4 was implemented in a way equivalent to what is depicted in fig. 16. Namely, it is the potential of HCl in the  $A^1\Pi$  excited state turned into a function of  $R_3$ . By using again  $R_3 \approx R_{\text{OH}_a}$  and  $R_{\text{H}_a\text{Cl}} + R_{\text{OH}_a} = \text{constant}$ , the  $A^1\Pi$  state potential was flipped (so that it decreases when  $R_3$  decreases) and translated in such a way that the Franck-Condon point corresponds to the expectation value  $\langle R_3 \rangle_0 = 4.0 a_0$  in the initial state. As was done for CAP ‘3’ for the other propagations, this repulsive potential was not activated until  $t = 6$  fs. This enables direct comparison with the main propagation discussed in section 6.1, as the initial conditions are identical.

### Notes and references

- 1 N. E. Henriksen and F. Y. Hansen, *Theories of Molecular Reaction Dynamics: The Microscopic Foundation of Chemical Kinetics*, Oxford University Press, 2nd edn, 2018.
- 2 D. R. Herschbach, *Angew. Chem. Int. Ed.*, 1987, **26**, 1221–1243.
- 3 U. Gerlach-Meyer, K. Kleinermanns, E. Linnebach and J. Wolfrum, *J. Chem. Phys.*, 1987, **86**, 3047.
- 4 C. Xiao, X. Xu, S. Liu, T. Wang, W. Dong, T. Yang, Z. Sun, D. Dai, X. Xu, D. H. Zhang and X. Yang, *Science*, 2011, **333**, 440–442.
- 5 T. Yang, J. Chen, L. Huang, T. Wang, C. Xiao, Z. Sun, D. Dai, X. Yang and D. H. Zhang, *Science*, 2015, **347**, 60–63.
- 6 D. M. Neumark, *Ann. Rev. Phys. Chem.*, 1992, **43**, 153–176.
- 7 D. M. Neumark, *Science*, 1996, **272**, 1446–1447.
- 8 C. Jouvet and B. Soep, *Chem. Phys. Lett.*, 1983, **96**, 426–428.
- 9 S. Buelow, G. Radhakrishnan, J. Catanzarite and C. Wittig, *J. Chem. Phys.*, 1985, **83**, 444–445.
- 10 G. Radhakrishnan, S. Buelow and C. Wittig, *J. Chem. Phys.*, 1986, **84**, 727–738.
- 11 J. Rice, G. Hoffmann and C. Wittig, *J. Chem. Phys.*, 1988, **88**, 2841.
- 12 Y. Chen, G. Hoffmann, D. Oh and C. Wittig, *Chem. Phys. Lett.*, 1989, **159**, 426–434.
- 13 E. Böhmer, S. K. Shin, Y. Chen and C. Wittig, *J. Chem. Phys.*, 1992, **97**, 2536–2547.
- 14 E. Böhmer, K. Mikhaylichenko and C. Wittig, *J. Chem. Phys.*, 1993, **99**, 6545–6552.
- 15 N. F. Scherer, L. R. Khundkar, R. B. Bernstein and A. H. Zewail, *J. Chem. Phys.*, 1987, **87**, 1451.
- 16 N. F. Scherer, C. Sipes, R. B. Bernstein and A. H. Zewail, *J. Chem. Phys.*, 1990, **92**, 5239–5259.
- 17 M. Gruebele, I. R. Sims, E. D. Potter and A. H. Zewail, *J. Chem. Phys.*, 1991, **95**, 7763–7766.
- 18 I. R. Sims, M. Gruebele, E. D. Potter and A. H. Zewail, *J. Chem. Phys.*, 1992, **97**, 4127–4148.

- 19 S. I. Ionov, G. A. Brucker, C. Jaques, L. Valachovic and C. Wittig, *J. Chem. Phys.*, 1992, **97**, 9486.
- 20 S. I. Ionov, P. I. Ionov and C. Wittig, *Faraday Discuss. Chem. Soc.*, 1994, **97**, 391.
- 21 C. Jaques, L. Valachovic, S. Ionov, E. Böhmer, Y. Wen, J. Segall and C. Wittig, *J. Chem. Soc. Faraday. Trans.*, 1993, **89**, 1419–1425.
- 22 S. A. Wright, M. F. Tuchler and J. McDonald, *Chem. Phys. Lett.*, 1994, **226**, 570–576.
- 23 M. F. Tuchler, S. Wright and J. D. McDonald, *J. Chem. Phys.*, 1997, **106**, 2634–2645.
- 24 R. Wester, A. E. Bragg, A. V. Davis and D. M. Neumark, *J. Chem. Phys.*, 2003, **119**, 10032–10039.
- 25 P. Y. Cheng, D. Zhong and A. H. Zewail, *J. Chem. Phys.*, 1995, **103**, 5153–5156.
- 26 D. Zhong, S. Ahmad, P. Y. Cheng and A. H. Zewail, *J. Am. Chem. Soc.*, 1997, **119**, 2305–2306.
- 27 O. K. Abou-Zied and J. D. McDonald, *J. Chem. Phys.*, 1998, **109**, 1293–1301.
- 28 P. Farmanara, V. Stert, W. Radloff, S. Skowronek and A. Gonzalez-Ureña, *Chem. Phys. Lett.*, 1999, **304**, 127–133.
- 29 V. Stert, P. Farmanara, W. Radloff, F. Noack, S. Skowronek, J. Jimenez and A. González Ureña, *Phys. Rev. A*, 1999, **59**, R1727–R1730.
- 30 V. Stert, P. Farmanara, H.-H. Ritze, W. Radloff, K. Gasmi and A. Gonzalez-Ureña, *Chem. Phys. Lett.*, 2001, **337**, 299–305.
- 31 B. Fu and D. H. Zhang, *J. Chem. Phys.*, 2012, **136**, 194301.
- 32 B. Fu and D. H. Zhang, *J. Phys. Chem. A*, 2012, **116**, 820–825.
- 33 B. Fu, Y. Zhou and D. H. Zhang, *Chem. Sci.*, 2012, **3**, 270–274.
- 34 B. Fu and D. H. Zhang, *J. Chem. Phys.*, 2013, **138**, 184308.
- 35 D. H. Zhang, M. Yang and S.-Y. Lee, *J. Chem. Phys.*, 2001, **114**, 8733–8736.
- 36 D. H. Zhang, M. Yang and S.-Y. Lee, *Phys. Rev. Lett.*, 2002, **89**, 103201.
- 37 A. Sinha, M. C. Hsiao and F. F. Crim, *J. Chem. Phys.*, 1990, **92**, 6333–6335.
- 38 A. Sinha, M. C. Hsiao and F. F. Crim, *J. Chem. Phys.*, 1991, **94**, 4928–4935.
- 39 R. B. Metz, J. D. Thoemke, J. M. Pfeiffer and F. F. Crim, *J. Chem. Phys.*, 1993, **99**, 1744–1751.
- 40 M. J. Bronikowski, W. R. Simpson, B. Girard and R. N. Zare, *J. Chem. Phys.*, 1991, **95**, 8647–8648.
- 41 M. J. Bronikowski, W. R. Simpson and R. N. Zare, *J. Chem. Phys.*, 1993, **97**, 2194–2203.
- 42 M. J. Bronikowski, W. R. Simpson and R. N. Zare, *J. Chem. Phys.*, 1993, **97**, 2204–2208.
- 43 N. E. Henriksen, *Chem. Phys.*, 2014, **442**, 2–8.
- 44 Z. Kisiel, E. Białkowska-Jaworska, L. Pszczółkowski, A. Milet, C. Struniewicz, R. Moszynski and J. Sadlej, *J. Chem. Phys.*, 2000, **112**, 5767–5776.
- 45 Z. Kisiel, B. A. Pietrewicz, P. W. Fowler, A. C. Legon and E. Steiner, *J. Phys. Chem. A*, 2000, **104**, 6970–6978.
- 46 A. C. Legon and L. C. Willoughby, *Chem. Phys. Lett.*, 1983, **95**, 449–452.
- 47 M. Fárník, M. Weimann and M. A. Suhm, *J. Chem. Phys.*, 2003, **118**, 10120–10136.
- 48 M. Weimann, M. Fárník and M. A. Suhm, *PCCP*, 2002, **4**, 3933–3937.
- 49 B. S. Ault and G. C. Pimentel, *J. Chem. Phys.*, 1973, **77**, 57–61.
- 50 G. P. Ayers and A. D. E. Pullin, *Spectrochimica Acta part A*, 1976, **32**, 1641–1650.
- 51 C. Amirand and D. Maillard, *J. Mol. Struct.*, 1988, **176**, 181–201.
- 52 A. Engdahl and B. Nelander, *J. Chem. Phys.*, 1986, **84**, 1981–1987.
- 53 A. J. Barnes, *J. Mol. Struct.*, 1983, **100**, 259–280.
- 54 A. Schriver, B. Silvi, D. Maillard and J. P. Perchard, *J. Chem. Phys.*, 1977, **81**, 2095–2102.
- 55 S. D. Flynn, D. Skvortsov, A. M. Morrison, T. Liang, M. Y. Choi, G. E. Douberly and A. F. Vilesov, *J. Phys. Chem. Lett.*, 2010, **1**, 2233–2238.
- 56 A. M. Morrison, S. D. Flynn, T. Liang and G. E. Douberly, *J. Phys. Chem. A*, 2010, **114**, 8090–8098.
- 57 M. Ortlieb, Ö. Birer, M. Letzner, G. W. Schwaab and M. Havenith, *J. Phys. Chem. A*, 2007, **111**, 12192–12199.
- 58 B. E. Casterline, A. K. Mollner, L. C. Ch'Ng and H. Reisler, *J. Phys. Chem. A*, 2010, **114**, 9774–9781.
- 59 B. E. Rocher-Casterline, A. K. Mollner, L. C. Ch'Ng and H. Reisler, *J. Phys. Chem. A*, 2011, **115**, 6903–6909.
- 60 A. J. Huneycutt, R. J. Stickland, F. Hellberg and R. J. Saykally, *Methods for Ultrasensitive Detection II*, 2002, **4634**, 70.
- 61 A. J. Huneycutt, R. J. Stickland, F. Hellberg and R. J. Saykally, *J. Chem. Phys.*, 2003, **118**, 1221–1229.
- 62 M. E. Alikhani and B. Silvi, *PCCP*, 2003, **5**, 2494–2498.
- 63 M. J. Packer and D. C. Clary, *J. Chem. Phys.*, 1995, **99**, 14323–14333.
- 64 Z. Latajka and S. Scheiner, *J. Chem. Phys.*, 1987, **87**, 5928–5936.
- 65 M. M. Szcześniak, S. Scheiner and Y. Bouteiller, *J. Chem. Phys.*, 1984, **81**, 5024–5030.
- 66 Y. Hannachi, B. Silvi and Y. Bouteiller, *J. Chem. Phys.*, 1991, **94**, 2915–2922.
- 67 S. Re, Y. Osamura, Y. Suzuki and H. F. Schaefer, *J. Chem. Phys.*, 1998, **109**, 973–977.
- 68 G. M. Chaban, R. B. Gerber and K. C. Janda, *J. Phys. Chem. A*, 2001, **105**, 8323–8332.
- 69 E. M. Cabaleiro-Lago, J. M. Hermida-Ramón and J. Rodríguez-Otero, *J. Chem. Phys.*, 2002, **117**, 3160–3168.
- 70 S. Odde, B. J. Mhin, S. Lee, H. M. Lee and K. S. Kim, *J. Chem. Phys.*, 2004, **120**, 9524–9535.
- 71 X. Zhang, Y. Zeng, X. Li, L. Meng and S. Zheng, *J. Mol. Struct. (Theochem)*, 2010, **950**, 27–35.

- 72 H. Liu, R. Man, Z. Wang, J. Liao, X. Li, S. Ma and P. Yi, *J. Theo. Comp. Chem.*, 2014, **13**, 1450037.
- 73 J. S. Mancini and J. M. Bowman, *J. Chem. Phys.*, 2013, **138**, 121102.
- 74 J. S. Mancini and J. M. Bowman, *J. Phys. Chem. Lett.*, 2014, **5**, 2247–2253.
- 75 J. S. Mancini and J. M. Bowman, *PCCP*, 2015, **17**, 6222–6226.
- 76 Y. Liu, J. Li, P. M. Felker and Z. Bačić, *PCCP*, 2021, **23**, 7101–7114.
- 77 J. A. Schmidt, M. S. Johnson, M. M. Grage and G. Nyman, *Chem. Phys. Lett.*, 2009, **480**, 168–172.
- 78 K. K. Irikura, *J. Phys. Chem. Ref. Data*, 2007, **36**, 389–397.
- 79 F. Gatti and C. Iung, *Phys. Rep.*, 2009, **484**, 1–69.
- 80 R. Radau, *Annales Scientifiques de l'Ecole Normale Supérieure*, 1868, **5**, 311–375.
- 81 F. T. Smith, *Phys. Rev. Lett.*, 1980, **45**, 1157–1160.
- 82 G. Brocks, A. V. D. Avoird, B. T. Sutcliffe and J. Tennyson, *Mol. Phys.*, 1983, **50**, 1025.
- 83 M. J. Bramley and T. Carrington, Jr., *J. Chem. Phys.*, 1993, **99**, 8519.
- 84 F. Gatti, C. Iung, M. Menou, Y. Justum, A. Nauts and X. Chapuisat, *J. Chem. Phys.*, 1998, **108**, 8804.
- 85 F. Gatti, *J. Chem. Phys.*, 1999, **111**, 7225.
- 86 A. Nauts and X. Chapuisat, *Mol. Phys.*, 1985, **55**, 1287–1318.
- 87 H. Essén, *Am. J. Phys.*, 1978, **46**, 983–988.
- 88 A. Nauts and F. Gatti, *Am. J. Phys.*, 2010, **78**, 1365–1375.
- 89 H.-D. Meyer, U. Manthe and L. S. Cederbaum, *Chem. Phys. Lett.*, 1990, **165**, 73–78.
- 90 U. Manthe, H.-D. Meyer and L. S. Cederbaum, *J. Chem. Phys.*, 1992, **97**, 3199–3213.
- 91 U. Manthe, H.-D. Meyer and L. S. Cederbaum, *J. Chem. Phys.*, 1992, **97**, 9062–9071.
- 92 M. Beck, A. Jäckle, G. A. Worth and H.-D. Meyer, *Phys. Rep.*, 2000, **324**, 1–105.
- 93 F. Gatti, B. Lasorne, H.-D. Meyer and A. Nauts, *Applications of Quantum Dynamics in Chemistry*, Springer International Publishing, 2017, vol. 98, pp. XIV, 429.
- 94 G. A. Worth, M. H. Beck, A. Jäckle, O. Vendrell and H.-D. Meyer, The MCTDH Package, Version 8.2, (2000). H.-D. Meyer, Version 8.3 (2002), Version 8.4 (2007). O. Vendrell and H.-D. Meyer Version 8.5 (2013). Version 8.5 contains the ML-MCTDH algorithm. Used version: 8.5.11 (2019). See <http://mctdh.uni-hd.de/>.
- 95 M. Abramowitz and I. Stegun, *Handbook of Mathematical Functions*, Dover Publ., 1973.
- 96 H.-D. Meyer, F. Le Quéré, C. Léonard and F. Gatti, *Chem. Phys.*, 2006, **329**, 179–192.
- 97 A. Jäckle and H. Meyer, *J. Chem. Phys.*, 1996, **104**, 7974–7984.
- 98 A. Jäckle and H.-D. Meyer, *J. Chem. Phys.*, 1998, **109**, 3772–3779.
- 99 F. Gatti and H.-D. Meyer, *Chem. Phys.*, 2004, **304**, 3–15.
- 100 J. Chen, X. Xu, X. Xu and D. H. Zhang, *J. Chem. Phys.*, 2013, **138**, 154301.
- 101 U. V. Riss and H.-D. Meyer, *J. Phys. B*, 1993, **26**, 4503.
- 102 U. V. Riss and H. D. Meyer, *J. Phys. B*, 1995, **28**, 1475–1493.
- 103 U. V. Riss and H. Meyer, *J. Chem. Phys.*, 1996, **105**, 1409–1419.
- 104 W. H. Miller, S. D. Schwartz and J. W. Tromp, *J. Chem. Phys.*, 1983, **79**, 4889–4898.
- 105 J. Tennyson, P. F. Bernath, L. R. Brown, A. Campargue, A. G. Császár, L. Daumont, R. R. Gamache, J. T. Hodges, O. V. Naumenko, O. L. Polyansky, L. S. Rothman, R. A. Toth, A. C. Vandaele, N. F. Zobov, S. Fally, A. Z. Fazliev, T. Furtenbacher, I. E. Gordon, S.-M. Hu, S. N. Mikhailenko and B. A. Voronin, *J. Quant. Spectrosc. Radiat. Transfer*, 2010, **111**, 2160–2184.
- 106 M. J. Frisch, G. W. Trucks, H. B. Schlegel, G. E. Scuseria, M. A. Robb, J. R. Cheeseman, G. Scalmani, V. Barone, G. A. Petersson, H. Nakatsuji, X. Li, M. Caricato, A. V. Marenich, J. Bloino, B. G. Janesko, R. Gomperts, B. Mennucci, H. P. Hratchian, J. V. Ortiz, A. F. Izmaylov, J. L. Sonnenberg, D. Williams-Young, F. Ding, F. Lipparini, F. Egidi, J. Goings, B. Peng, A. Petrone, T. Henderson, D. Ranasinghe, V. G. Zakrzewski, J. Gao, N. Rega, G. Zheng, W. Liang, M. Hada, M. Ehara, K. Toyota, R. Fukuda, J. Hasegawa, M. Ishida, T. Nakajima, Y. Honda, O. Kitao, H. Nakai, T. Vreven, K. Throssell, J. A. Montgomery, Jr., J. E. Peralta, F. Ogliaro, M. J. Bearpark, J. J. Heyd, E. N. Brothers, K. N. Kudin, V. N. Staroverov, T. A. Keith, R. Kobayashi, J. Normand, K. Raghavachari, A. P. Rendell, J. C. Burant, S. S. Iyengar, J. Tomasi, M. Cossi, J. M. Millam, M. Klene, C. Adamo, R. Cammi, J. W. Ochterski, R. L. Martin, K. Morokuma, O. Farkas, J. B. Foresman and D. J. Fox, *Gaussian 16 Revision C.01*, 2016, Gaussian Inc. Wallingford CT.
- 107 D. F. Dinu, M. Podewitz, H. Grothe, K. R. Liedl and T. Loerting, *J. Phys. Chem. A*, 2019, **123**, 8234–8242.
- 108 M. Yang, D. H. Zhang, M. A. Collins and S.-Y. Lee, *J. Chem. Phys.*, 2001, **115**, 174–178.
- 109 F. Fernández-Alonso and R. N. Zare, *Ann. Rev. Phys. Chem.*, 2002, **53**, 67–99.
- 110 T. Furtenbacher, A. G. Császár and J. Tennyson, *J. Mol. Spec.*, 2007, **245**, 115 – 125.
- 111 T. Furtenbacher and A. G. Császár, *J. Mol. Struct.*, 2012, **1009**, 123 – 129.
- 112 T. Furtenbacher and A. G. Császár, *J. Quant. Spectrosc. Radiat. Transfer*, 2012, **113**, 929 – 935.